

The GAPS Programme with HARPS-N at TNG

XXXI. The WASP-33 system revisited with HARPS-N[★]

F. Borsa¹, A. F. Lanza², I. Raspantini³, M. Rainer⁴, L. Fossati⁵, M. Brogi^{6,7,8}, M. P. Di Mauro⁹, R. Gratton¹⁰, L. Pino⁴, S. Benatti¹¹, A. Bignamini¹², A. S. Bonomo⁷, R. Claudi¹⁰, M. Esposito¹³, G. Frustagli^{3,1}, A. Maggio¹¹, J. Maldonado¹¹, L. Mancini^{14,15,7}, G. Micela¹¹, V. Nascimbeni¹⁰, E. Poretti^{1,16}, G. Scandariato², D. Sicilia², A. Sozzetti⁷, W. Boschin^{16,17,18}, R. Cosentino¹⁶, E. Covino¹⁹, S. Desidera¹⁰, L. Di Fabrizio¹⁶, A. F. M. Fiorenzano¹⁶, A. Harutyunyan¹⁶, C. Knapic¹², E. Molinari²⁰, I. Pagano², M. Pedani¹⁶, G. Piotto²¹

(Affiliations can be found after the references)

Received ; accepted

ABSTRACT

Context. Giant planets in short-period orbits around bright stars represent optimal candidates for atmospheric and dynamical studies of exoplanetary systems.

Aims. We analyse four transits of WASP-33b observed with the optical high-resolution HARPS-N spectrograph to confirm its nodal precession, study its atmosphere and investigate the presence of star-planet interactions.

Methods. We extract the mean line profiles of the spectra by using the Least Square Deconvolution method, and analyse the Doppler shadow and the radial velocities. We also derive the transmission spectrum of the planet, correcting it for the stellar contamination due to rotation, center-to-limb variations and pulsations.

Results. We confirm the previously discovered nodal precession of WASP-33b, almost doubling the time coverage of the inclination and projected spin-orbit angle variation. We find that the projected obliquity reached a minimum in 2011 and use this constraint to derive the geometry of the system, in particular its obliquity at that epoch ($\epsilon = 113.99^\circ \pm 0.22^\circ$) and the inclination of the stellar spin axis ($i_s = 90.11^\circ \pm 0.12^\circ$), as well as the gravitational quadrupole moment of the star $J_2 = (6.73 \pm 0.22) \times 10^{-5}$, that we find to be in close agreement with the theoretically predicted value. Small systematic errors are computed by shifting the date of the minimum projected obliquity. We present detections of H α and H β absorption in the atmosphere of the planet, with a contrast almost twice smaller than previously detected in the literature. We also find evidence for the presence of a pre-transit signal, which repeats in all four analysed transits and should thus be related to the planet. The most likely explanation lies in a possible excitation of a stellar pulsation mode by the presence of the planetary companion.

Conclusions. A future common analysis of all available datasets in the literature will help shedding light on the possibility that the observed Balmer lines transit depth variations are related to stellar activity and/or pulsation, and to set constraints on the planetary temperature-pressure structure and thus on the energetics possibly driving atmospheric escape. A complete orbital phase coverage of WASP-33b with high-resolution spectroscopic (and spectro-polarimetric) observations could help understanding the nature of the pre-transit signal.

Key words. planetary systems – techniques: spectroscopic – techniques: radial velocities – planets and satellites: atmospheres – stars:individual:WASP-33

1. Introduction

Transiting exoplanets orbiting intermediate mass (e.g., A-type) stars on short period ($P_{\text{orb}} \leq 5$ days) orbits are excellent laboratories for atmospheric and dynamical studies. The high day-side equilibrium temperatures of these Ultra-Hot Jupiters (UHJs, $T_{\text{eq}} \geq 2200$ K) cause the thermal dissociation of most molecules (e.g., Lothringer et al. 2018; Arcangeli et al. 2018). Depending on the heat transfer efficiency in the atmosphere there might be also variations in the chemical composition of the day-side, night-side and terminator of the planet (e.g., Parmentier et al. 2018). Orbiting at short distances from their parent star, the strong stellar ultraviolet irradiation makes the planetary atmo-

sphere undergoing a significant mass loss, affecting its composition and evolution (e.g., Fossati et al. 2018).

Short-period systems are interesting also because they experience strong tidal interactions between the planet and its host star. Star-planet tidal interactions could modify the stellar rotation rate along the system's evolution (Gallet et al. 2018), cause planet oblateness (Akisanmi et al. 2019), suppress stellar activity (Fossati et al. 2018), and/or induce stellar pulsations (de Wit et al. 2017). The measure of the projected spin-orbit angle either with radial velocities (RVs) through the Rossiter-McLaughlin effect (RM, Rossiter 1924; McLaughlin 1924) or with the Doppler tomography technique (e.g., Collier Cameron et al. 2010) can help to shed light on a system evolution history (e.g., Fabrycky & Winn 2009).

In this context, WASP-33b (Collier Cameron et al. 2010) is a very intriguing target. It is a UHJ ($M_p \sim 2.2 M_{\text{Jup}}$, $R_p \sim 1.6 R_{\text{Jup}}$) orbiting in ~ 1.21 days a bright δ -Scuti A-type star ($V=8.3$, $T_{\text{eff}} \sim 7500$ K, $v \sin i_s \sim 86$ km s⁻¹) with a highly misaligned projected spin-orbit angle $\lambda \sim -110$ degrees (Collier Cameron et al. 2010; Lehmann et al. 2015). Stellar non-radial pulsations were

Send offprint requests to: F. Borsa
e-mail: francesco.borsa@inaf.it

[★] Based on observations made with the Italian Telescopio Nazionale Galileo (TNG) operated on the island of La Palma by the Fundacion Galileo Galilei of the INAF at the Spanish Observatorio Roque de los Muchachos of the IAC in the frame of the program Global Architecture of the Planetary Systems (GAPS).

already noted spectroscopically in the discovery paper (Collier Cameron et al. 2010). Photometric oscillations of the star were first reported by Herrero et al. (2011), and the stellar pulsation spectrum has been analysed in different studies (Kovács et al. 2013; von Essen et al. 2014; Mkrichian 2015; von Essen et al. 2020). Because of its easily detected stellar pulsations, the WASP-33 system has been considered a good candidate for the detection of star-planet interactions (Herrero et al. 2011). WASP-33b was also noted as a possible target for which both classical and relativistic node precessional effects could be evidenced within a reasonable amount of time (Iorio 2011, 2016); indeed classical node precessional effects have been afterwards detected by Johnson et al. (2015) and Watanabe et al. (2020).

Its atmosphere has also been the subject of different studies. The probable presence of a temperature inversion in its atmosphere (Haynes et al. 2015; von Essen et al. 2015) was best explained by the presence of titanium oxide (TiO), whose detection with high-resolution spectroscopy is however debated (Nugroho et al. 2017; Herman et al. 2020). Other results include the first indication of aluminum oxide (AlO) in an exoplanet by using low resolution spectrophotometry (von Essen et al. 2019), the detection of ionized calcium (Ca II H&K) up to very high upper-atmosphere layers close to the planetary Roche lobe (Yan et al. 2019) and of Balmer lines (Yan et al. 2021; Cauley et al. 2021). The existence of a thermal inversion was recently confirmed with the detection of Fe I in emission using high-resolution observations (Nugroho et al. 2020).

Driven by the intriguing characteristics of the system, in this work we analyse new transits of WASP-33b taken with the HARPS-N high-resolution spectrograph, looking for confirmation of the nodal precession and exploring its atmosphere. This manuscript is organized as follows. We first present our data in Sect. 2, then analyse the planetary Doppler shadow and the in-transit RVs studying also the precession of the orbital plane and of the spin of the host star (Sect. 3 and 4). We study the planetary atmosphere focusing on H α and H β absorption in Sect. 5, finding a pre-transit signal coherent with the planetary orbital period discussed in Sect. 6. Then we look for other atmospheric species with the cross-correlation technique in Sect. 7, ending with summary and conclusions in Sect. 8.

2. Data sample

We observed WASP-33 during four transits using the high-resolution (resolving power $R \sim 115000$) HARPS-N spectrograph (Cosentino et al. 2012), mounted at the Telescopio Nazionale Galileo on the La Palma island and covering the wavelength range 380-690 nm. The first two transits were observed with HARPS-N only (program A34TAC42, PI Nascimbeni), while the other two were taken in the framework of the GAPS project (Covino et al. 2013). The latter were observed using the GIARPS configuration (Claudi et al. 2017), but in this manuscript we focus only on the HARPS-N data.

The transit of WASP-33b lasts 2 hours 48 minutes. Three transit observations were monitored with exposures of 600 sec, while for one we used a longer cadence (900 sec exposures). While the fiber A of the spectrograph was centered on the target, for all the transits the fiber B was monitoring simultaneously the sky to check for possible atmospheric emission contamination. The log of the observations is reported in Table 1.

The quality of transit 2 rapidly decreases after the transit ingress due to weather conditions, we thus decided to not include it in the analysis of the transmission spectrum, Doppler shadow

Table 1. WASP-33 HARPS-N observations log.

Transit number	Night ¹	Exposure time	N _{obs}	S/N _{ave}
1	28 Sep 2016	600s	40	107
2*	20 Oct 2016	600s	32	90
3	12 Jan 2018	900s	23	166
4	02 Jan 2019	600s	33	115

*Weather conditions rapidly worsening.

¹Start of night civil date.

and RVs, but only in Sect. 6 where we look at the pre-transit portion of the data.

3. Precession of the orbital plane and stellar spin axis

WASP-33 is a δ -Sct A-type star. Since no default A-type mask is supported by the HARPS-N DRS pipeline (Cosentino et al. 2014), we followed the approach presented in Borsa et al. (2019) and extracted the mean line profiles by means of the Least Square Deconvolution (LSD) software (Donati et al. 1997). This software performs a Least-Squares Deconvolution of the normalised spectra with a theoretical line mask extracted from VALD (Vienna Atomic Line Database, Piskunov et al. 1995). We used a stellar mask with $T_{\text{eff}}=7500$ K, $\log g=4.0$, and solar metallicity. We accurately re-normalised the spectra (order-by-order by using polynomials, see Rainer et al. (2016) for a detailed description of the procedure) and converted them to the required format, working only on the wavelength regions 441.5 – 480.5 nm, 491.5 – 528.5 nm, 536.5 – 587.0 nm, 605.0 – 626.5 nm, and 633.5 – 645.0 nm, i.e., cutting the blue orders where the signal-to-noise ratio (S/N) was very low due to the instrument efficiency, the Balmer lines, and the regions where most of the telluric lines are found. We then created mean line profile residuals by dividing all the mean line profiles by a master out-of-transit mean line profile for each transit observed. As already evidenced by Collier Cameron et al. (2010) and Johnson et al. (2015), the Doppler shadow of the planet is clearly visible as well as the stellar pulsations (Fig. 1, left panel). We note that the pulsations are more evident on the edge of the lines with respect to the center, which is a hint of non-radial pulsations (see also Collier Cameron et al. 2010).

For planets with projected spin-orbit angles close to 90 deg, nodal precession can be more easily detected during observations spanning several years (Watanabe et al. 2020). WASP-33b is one of the two reported cases where the exoplanet orbit has been found to show nodal precession (Johnson et al. 2015; Watanabe et al. 2020), with the other case being Kepler-13Ab (Szabó et al. 2012; Herman et al. 2018). Since our dataset extends the timespan of the reported orbital variations, we tried to see if this was visible also in our data. We removed stellar pulsations independently for each single transit by using the Fourier transform filtering (Fig. 1), following the method presented in Johnson et al. (2015). This exploits the fact that pulsations (prograde) and Doppler shadow (retrograde) propagate in opposite directions: their frequency components thus tend to be separated in the two-dimensional Fourier transform of the line profile residuals time series (Johnson et al. 2015). We then performed a fit to the Doppler shadow. The Doppler shadow model is taken from EXOFASTv2 (Eastman 2017; Eastman et al. 2019), passed through the Fourier filter and fitted to the data in a Bayesian

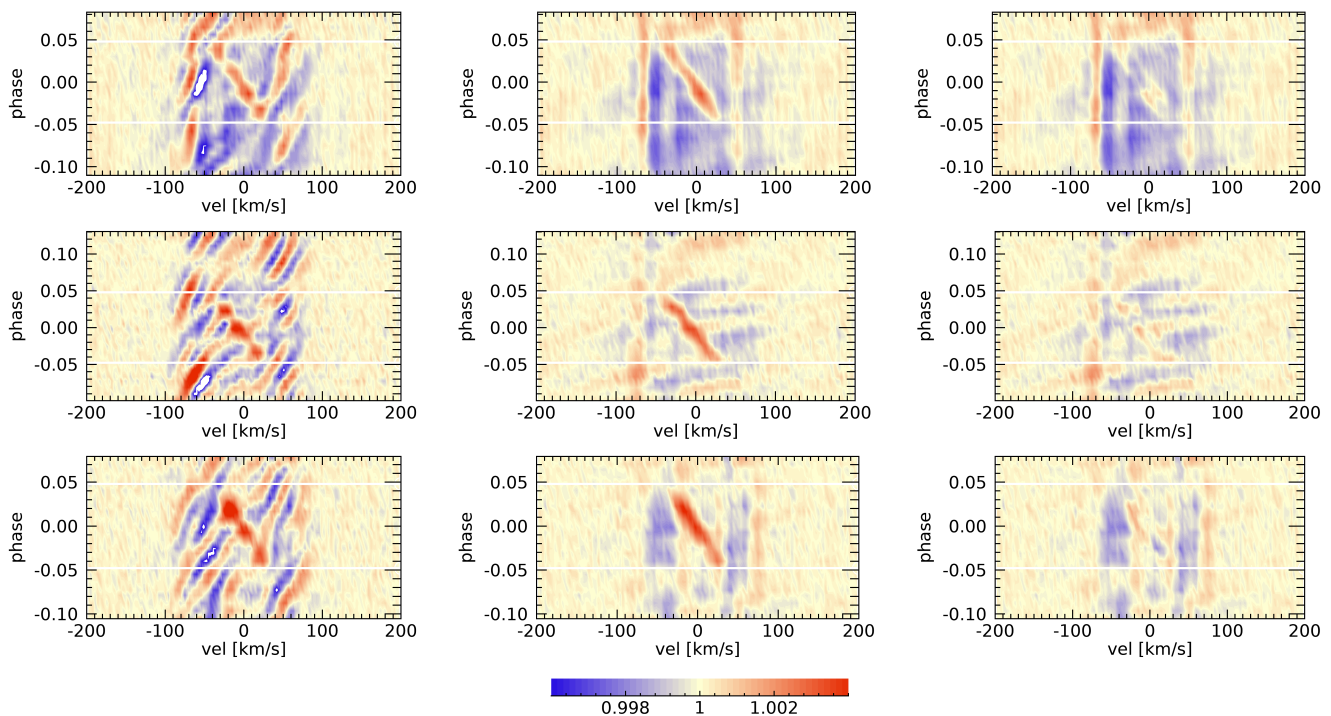


Fig. 1. Tomography of the pulsation filtering from the mean line profile residuals. From top to bottom: transits 1, 3 and 4, respectively. (*Left panels*): contour plot of the mean line profile residuals. (*Central panels*): same as for left panels, but after filtering in the Fourier space. (*Right panels*): same as for central panels, after subtracting the best fit Doppler shadow model. The horizontal white lines show the beginning and end of the transit.

framework by employing a differential evolution Markov chain Monte Carlo (DE-MCMC) technique (Ter Braak 2006; Eastman et al. 2013), running five DE-MCMC chains of 100,000 steps and discarding the burn-in. We fixed $v \sin i_s$, a/R_s , T_0 , period, R_p/R_s to the values of Table 2. We left as free parameters the projected spin-orbit angle λ and the inclination angle i , for which we set uninformative priors. The medians and the 15.86% and 84.14% quantiles of the posterior distributions were taken as the best values and 1σ uncertainties.

Our results (Fig. 2, Table 2), together with the previous measurements of Watanabe et al. (2020), confirm the precession of the planetary orbit and that the obliquity projected on the plane of the sky λ reached a minimum in 2011. This allows us to determine the inclination of the stellar spin axis to the line of sight i_s and the obliquity ϵ at the epoch when $d\lambda/dt = 0$, thus allowing a more precise description of the precession of the system and the measure of the stellar gravitational quadrupole moment J_2 . We describe the method applied to determine the system geometry as well as the rate of precession of the nodes of the orbital plane in Appendix A.

The rate of change of the inclination angle of the orbital plane i can be regarded as constant over the time span of the observations (~ 10 yr) because it is much shorter than the precession period (~ 1100 yr; see below). It is measured by a weighted linear best fit to the data in Fig. 2 (upper panel) giving $di/dt = 0.324 \pm 0.006$ deg/yr, while the epoch when $d\lambda/dt = 0$ is assumed to coincide with the transit observed on 19 October 2011, when $i = 87.56^\circ \pm 0.037^\circ$ and $\lambda = -114.01^\circ \pm 0.22^\circ$ (Watanabe et al. 2020). Given the uncertainty on such an epoch,

we report the systematic deviations in the derived model parameters corresponding to a shift of the epoch of $d\lambda/dt = 0$ by ± 500 days since the assumed epoch, respectively (Table A.1). To compute these deviations, we assume that di/dt has the same value as above, while we linearly interpolate for the parameter i and cubically interpolate for the parameter λ to find their values at the two epochs. We report for each parameter the standard deviation as a measure of the statistical error, while we add in brackets the systematic deviation when $d\lambda/dt = 0$ at the later epoch and the deviation when $d\lambda/dt = 0$ at the earlier epoch, respectively. Note that the two deviations have the same sign when the parameter reached an extremum in between the considered epoches.

Following the method described in Appendix A, we find that the stellar spin is perpendicular to the line of sight ($i_s = 90.11^\circ \pm 0.12^\circ$ (-0.026° ; -0.015°)), while the obliquity $\epsilon = 113.99^\circ \pm 0.22^\circ$ (-0.24° ; -0.67°) at the epoch of the transit on 19 October 2011. From the spectroscopic stellar $v \sin i_s$, i_s , and stellar radius, we estimate a rotation period of the star of 0.884 ± 0.02 days, not significantly affected by the systematic errors on i_s because it is close to 90° . The precession rate of the nodes of the orbital plane is found to be -0.325 ± 0.006 (6.7×10^{-5} ; 1.1×10^{-4}) deg/yr giving a precession period of 1108 ± 19 (0.23; 0.38) yr, slightly longer than that determined by Johnson et al. (2015). The time interval during which transits by WASP-33b are observable is thus of ~ 97 yr centred around 2019, slightly longer than their interval of about ~ 88 yr.

Our inclination i_s of the stellar spin axis to the line of sight is different from the value found by Iorio (2016) because his determination was based on the parameters derived only from the

transits of 2008 and 2014 as reported by Johnson et al. (2015). This led Iorio to consider a constant precession rate of the angle I of his model, while our more extended dataset shows that dI/dt is variable and became zero around 2011. In Appendix A.5, we account for the differences between his results and ours and show how the application of his model to our dataset reproduces our value of i_s and of the stellar quadrupole moment (see below).

Previous analyses of the precession of WASP-33b by Johnson et al. (2015) and Watanabe et al. (2020) assumed that the stellar spin angular momentum is much larger than the orbital angular momentum because they adopted the gyration radius γ typical of a Sun-like star following the exploratory calculations by Iorio (2011). Here we determine more appropriate values of the gyration radius and apsidal motion constant k_2 of WASP-33 by making use of the tabulations of Claret (2019). Considering the uncertainties in the stellar mass and effective temperature, we find that the Claret’s model with solar metallicity and mass of $1.6 M_\odot$ is adequate to describe WASP-33. Taking into account the correction for its fast rotation, we find $\log k_2 = -2.55 \pm 0.014$ and $\gamma = 0.1884 \pm 0.0019$, where the uncertainties take into account only the uncertainty in the stellar effective temperature.

With the above values of k_2 , γ , and the adopted stellar and planetary parameters, we predict a value of $di/dt = 0.315 \pm 0.026$ (0.0023; 0.0068) deg/yr and a precession rate of the nodes of -0.316 ± 0.026 (0.0024; 0.0069) deg/yr using the formulae given in Appendix A.3. The coincidence of these numerical values comes from the geometry of the system as explained there. These precession rates differ by less than a half standard deviation from the observed ones, supporting the correctness of the adopted stellar parameters. With our value of γ and the adopted system parameters, we find that the ratio of the stellar spin to the orbital angular momentum is 2.75 ± 0.33 , therefore, we cannot neglect the precession of the stellar spin. It occurs with the same period as the precession of the node of the orbital plane and makes the inclination i_s of the stellar spin axis to the line of sight vary between 67.5° and 110.8° along a complete precession cycle. Note that an inclination of the stellar spin greater than 90° implies that the South pole of the star is in view, so the apparent stellar rotation is clockwise, contrary to the usual anticlockwise rotation assumed when $i_s < 90^\circ$ and the North pole is in view.

The fast stellar rotation produces a deformation in the stellar mass distribution and hence a distortion in the gravitational field. The stellar gravitational quadrupole moment J_2 can be deduced from the observed nodal precession rate of the orbital plane according to eq. (3) of Johnson et al. (2015) and is $(6.73 \pm 0.22 [0.062; 0.18]) \times 10^{-5}$. This value compares well with the theoretically expected value of $(6.53 \pm 0.41 [0.011; 0.031]) \times 10^{-5}$ (e.g., Ragozzine & Wolf 2009, and Appendix A.4), thus confirming the goodness of the adopted values of k_2 and γ . It also supports the hypothesis that WASP-33b is the only close massive planet in the system because another similar body would contribute to the orbital precession rate, if its orbit were not coplanar with that of WASP-33b. The fast rotation of WASP-33 makes its quadrupole moment ~ 375 times larger than the solar value ($J_{2\odot} \sim 1.8 \times 10^{-7}$; Rozelot et al. 2009), the effect of the centrifugal force being only modestly compensated by the stronger density concentration in an A-type star.

4. Radial velocities

Since we could not exploit the Cross-Correlation Functions (CCFs) from the DRS, RVs were extracted following the same method presented in Borsa et al. (2019). Instead of using a Gaussian fit, we preferred to model the LSD lines with a rotational

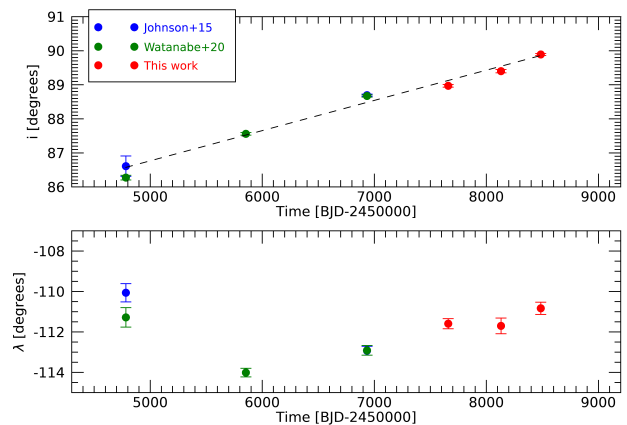


Fig. 2. Measurements of the inclination angle i (top panel) and of the projected spin-orbit angle λ (bottom panel) as a function of time. The dashed line shows the linear trend discussed in Sect. 3.

Table 2. Stellar and orbital parameters adopted in this work.

Parameter	Value	Reference
WASP-33		
<i>Stellar parameters</i>		
T_{eff} [K]	7430 ± 100	Yan et al. 2019
$\log g$	4.3 ± 0.2	Yan et al. 2019
$[Fe/H]$	-0.1 ± 0.2	Yan et al. 2019
R_s [R_\odot]	1.509 ± 0.025	Yan et al. 2019
M_s [M_\odot]	1.561 ± 0.06	Yan et al. 2019
$v \sin i_s$ [km s^{-1}]	86.4 ± 0.5	This work
P_{rot} [days]	0.884 ± 0.02	This work
<i>Orbital parameters</i>		
Period [days]	1.219870897	Yan et al. 2019
T_0 [BJD-2450000]	4163.22449	Yan et al. 2019
R_p/R_s	0.11177	Yan et al. 2019
a/R_s	3.69 ± 0.05	Yan et al. 2019
e	0.0	assumed
i [degrees]	88.97 ± 0.04	This work, transit 1
i [degrees]	89.40 ± 0.05	This work, transit 3
i [degrees]	89.89 ± 0.03	This work, transit 4
λ [degrees]	-111.59 ± 0.25	This work, transit 1
λ [degrees]	-111.70 ± 0.39	This work, transit 3
λ [degrees]	-110.83 ± 0.30	This work, transit 4
V_{sys} [km s^{-1}]	-2.76 ± 0.04	This work
K_p [km s^{-1}]	231 ± 3	Yan et al. 2019
M_p [M_{Jup}]	2.16 ± 0.20	Yan et al. 2019
T_{eq} [K]	2710 ± 50	Yan et al. 2019

profile (Gray 2008). We measured a $v \sin i_s = 86.4 \pm 0.5 \text{ km s}^{-1}$, taken as the average of the out-of-transit measurements and their standard deviation, which is well in agreement with previous values ($v \sin i_s = 86.63 \text{ km s}^{-1}$, Johnson et al. 2015). The extracted RVs are listed in Table B.1. We subtracted from each transit observation the difference from the mean of the in-transit RVs, to avoid any possible offset caused by instabilities, long-term pulsations and trends in the orbital solution (e.g., Borsa et al. 2019), and then averaged the RVs of the four transits in bins of 0.005 in phase. The RV time series of each single transit analysed and their average are shown in Fig. 3.

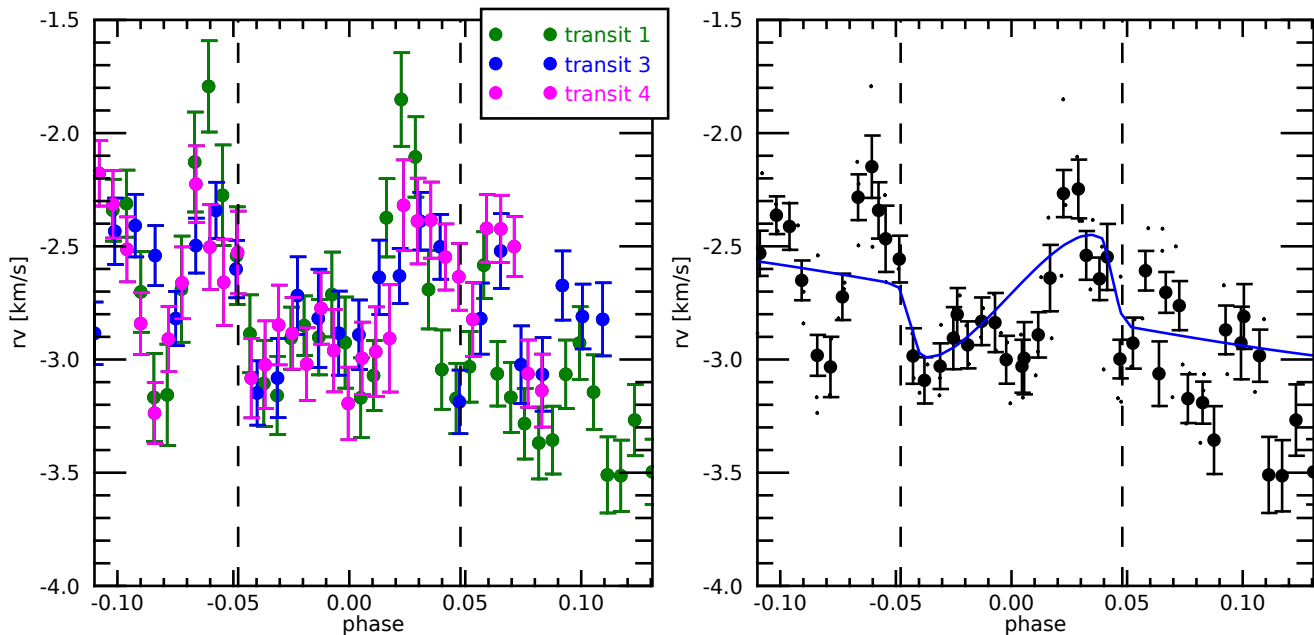


Fig. 3. (*Left panel*) Phase folded RVs of the three analysed HARPS-N transits of WASP-33b. Different colours refer to different transits. (*Right panel*) RVs of the three transits averaged in bins of 0.005 in phase (filled circles), together with single RVs (small dots). The blue line represents the theoretical RV solution calculated with the parameters of Table 2 (the values of λ and i are obtained from the average of the three transits).

Although stellar pulsations dominate also the RV curve, it is evident a qualitative agreement with the theoretical RM curve calculated using the parameters presented in Table 2 (by using the formalism of Ohta et al. 2005). This is a further confirmation that for fast rotators the method of fitting the mean line profiles with a rotational profile instead of a Gaussian function brings optimal results, as it was previously found for other targets (e.g., Anderson et al. 2018; Johnson et al. 2018; Borsa et al. 2019; Rainer et al. 2021). We note however that for this case the Doppler tomography method remains the preferred one to determine the projected spin-orbit inclination angle.

5. Balmer lines absorption in the transmission spectrum

We studied the atmosphere of WASP-33b by using the technique of transmission spectroscopy, focusing on $H\alpha$ and $H\beta$ absorption and taking into account the possible contamination given by stellar effects.

5.1. Transmission spectrum extraction

We performed transmission spectroscopy following the method of Wyttenbach et al. (2015), applying the following steps independently to each transit. First we shifted the spectra to the stellar radial velocity rest frame using a Keplerian model of the system. Then we normalized each spectrum, by dividing for the average flux within defined wavelength ranges where telluric and stellar lines are not present.

Using the out-of-transit spectra only, we built a telluric reference spectrum $T(\lambda)$, by means of a linear correlation between the logarithm of the normalized flux and the airmass (Snellen et al. 2008; Vidal-Madjar et al. 2010; Astudillo-Defru & Rojo 2013), and then rescaled all the spectra as if they had been observed at

the airmass corresponding to that at the center of the transit. We then created a master stellar spectrum S_{master} by averaging all the out-of-transit spectra (excluding the phase range of the immediate pre-transit, see Sect. 6), and divided all the single spectra for this S_{master} creating the residual spectra S_{res} . Every S_{res} was then shifted considering the theoretical planetary RV and the systemic velocity of the system, i.e., we placed the spectra in the planetary reference frame. Here we expect to detect the exoplanetary atmospheric signal centered at the laboratory wavelengths. All the full-in-transit S_{res} were then averaged to create the transmission spectrum. At this stage, the transmission spectrum of the planet still includes spurious stellar contaminations.

5.2. Removal of CLV + RM

The star over which the planet transits is not a simple homogeneous disk, but rotates and has a surface brightness which changes as a function of the distance from center. Effects such as center-to-limb variations (CLV) and RM have been proven to significantly modify the shape of line profiles, possibly causing false atmospheric detections (e.g., Yan et al. 2017; Borsa & Zannoni 2018; Casasayas-Barris et al. 2020). We thus took these effects into account by creating a model following the methodology described in Yan et al. (2017). The star is modeled as a disk divided in sections of $0.01 R_s$. For each point, we calculate the μ value (where $\mu = \cos \theta$, with θ the angle between the normal to the stellar surface and the line of sight) and the projected rotational velocity (by assuming rigid body rotation and rescaling the $v \sin i_s$ value of Table 2). A spectrum is then assigned to each point of the grid, by quadratically interpolating on μ and Doppler-shifting for the stellar rotation the model spectra created using the tool Spectroscopy Made Easy (SME, Piskunov & Valenti 2017), with the line list from the VALD database (Ryabchikova et al. 2015) and the MARCS (Gustaf-

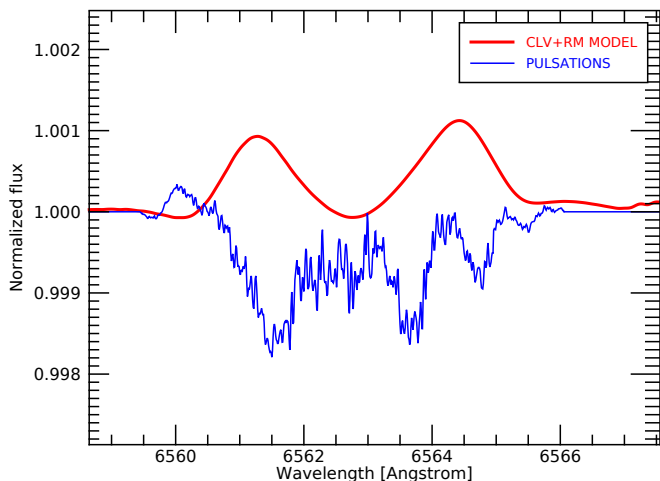


Fig. 4. The corrections for CLV+RM and for stellar pulsations applied to the transmission spectrum in the $H\alpha$ zone.

son et al. 2008) stellar atmospheric models (assuming local thermodynamic equilibrium approximation). The model spectra are created with null rotational velocity for 21 different μ values, and adapted to the resolving power of the instrument. Then, using the orbital information from Table 2 we simulate the transit of the planet, calculating the stellar spectrum for different orbital phases as the average spectrum of the non-occulted modeled sections. As the last step, we divide each spectrum for a master stellar spectrum calculated out-of-transit, obtaining the information of the impact of RM+CLV effects at each in-transit orbital phase. We then move everything in the planetary restframe and calculate the simulated CLV+RM effects on the transmission spectrum (Fig. 4). We note that we do not take into account the possible deformation of the line profiles given by gravity darkening, which are however not expected to be significant (see, e.g., Kovács et al. 2013).

5.3. Removal of pulsations

Another contamination one has to deal with in this particular case of WASP-33b comes from the stellar pulsations. We already showed in Sect. 3 how strongly they impact the mean line profiles. In the same way, they will have an impact in the extracted planetary transmission spectrum. To deal with this, we used an approach similar to that presented in Borsa & Zannoni (2018) to remove the RM from the transmission spectrum by using real observing data. This was done by exploiting the S/N of the mean line profiles. We note that pulsations and RM cannot be removed together in this way. This is because the amplitude of the RM effect is dependent on the planetary effective radius in the narrow bandpasses where the planetary lines are present. On the contrary, the amplitude of pulsations vary on a much larger wavelength range and can be assumed constant in each of our narrow bandpasses of interest. In the following, we make the assumption that the pulsation pattern behaves in the same way for all the absorption lines. We use the pulsation pattern extracted from the mean line profile (which is basically based on metal lines) and assume that it is valid also for the Balmer lines, except for a scaling factor. To justify this assumption we note that the short periods of δ Sct are not able to produce significant phase shifts between the photospheric stellar lines of different species and excitation potentials. Moreover, the broadening of the Balmer

lines largely affects the wings, but not so much the center, where we search for the in-transit planetary RVs: Balmer and metallic line-profiles are very similar there. We also note that we cannot analyse the pulsation pattern directly on the Balmer lines, due to their low S/N. As a final test we verified that the applied correction does not impact the depth of the retrieved planetary line-profile (Sect. 5.4).

We started from the mean line profiles residuals, after the division for an average out-of-transit mean line profile. We then subtracted for each transit the Doppler shadow models calculated in Sect. 3 (e.g., Fig. 5). Then we created a transmission spectrum of the pulsations (TS_{puls}) in the wavelength region of interest. First we put together the three transits, then we move from the velocity to the wavelength space, taking as zero reference the laboratory wavelength of the $H\alpha$ (Fig. 6) and $H\beta$ lines, since these are the lines we aim at correcting. Then we moved each mean line profile residual to the planetary restframe, and averaged the full-in-transit residuals to calculate the TS_{puls} . At this point we still have to correct for the magnitude of the effect: the calculated TS_{puls} is in fact referred to a line whose depth is the one of the mean line profile, and has to be rescaled to the depth of the line that we want to correct (Borsa & Zannoni 2018). We thus multiplied the amplitude of the correction for a factor which is the ratio between the depth of the mean line profile and that of the $H\alpha$ (or $H\beta$) line, and obtained the final spectrum used to correct for pulsations (Fig. 4).

5.4. Balmer lines absorption

We corrected the transmission spectrum extracted in Sect. 5.1 from stellar effects by dividing it for the corrective spectra calculated in Sect. 5.2 and 5.3. We note that the effect of pulsations overcomes that of CLV+RM by a factor ~ 1.5 in magnitude (Fig. 4). We find an excess absorption in the $H\alpha$ region with a contrast of $0.54 \pm 0.04\%$ and a FWHM of 36.7 ± 3.3 km s^{-1} (Fig. 7). We can translate the contrast into an effective planetary radius $R_{\text{eff}} = 1.18 \pm 0.02 R_p$, calculated assuming $R_{\text{eff}}^2/R_p^2 = (\delta + h)/\delta$, with δ the transit depth (from Table 2) and h the line contrast (e.g., Chen et al. 2020). As for KELT-9b, the $H\alpha$ profile of WASP-33b forms in the atmospheric region below the Roche lobe, which lies at about 1.6 planetary radii. Therefore this detection does not directly probe atmospheric escape, but it would enable one to set constraints on the planetary temperature-pressure structure and thus on the energetics possibly driving escape. The line has a significant blueshift of -8.2 ± 1.4 km s^{-1} , indicative of winds in the planetary atmosphere. We note that without the correction for the stellar pulsations we find a comparable depth (0.53%) but a larger FWHM (55 km s^{-1}). Being non-radial pulsations, their averaged effect on the three transits tends to be smaller in the center of the stellar line profile, and this is reflected also in the transmission spectrum. This is also noticeable in Fig. 4 and Fig. 6.

Checking the reference frame of the detections is fundamental when we want to be sure they are caused by the planetary atmosphere and not by spurious stellar effects (e.g., Brogi et al. 2016; Borsa & Zannoni 2018), in particular for this case where the strong stellar pulsations could be not perfectly corrected for and mimic atmospheric features. We thus verified that our $H\alpha$ absorption detection is in the planetary restframe by resolving it in the 2D tomographic map (Fig. 8), which shows the position of the absorption signal as a function of the orbital phase.

We also find an excess absorption in the $H\beta$ line region with a contrast of $0.28 \pm 0.06\%$, FWHM of 23.5 ± 6.3 km s^{-1} and a blueshift of -6.6 ± 2.6 km s^{-1} (Fig. 9 and Fig. 10). We

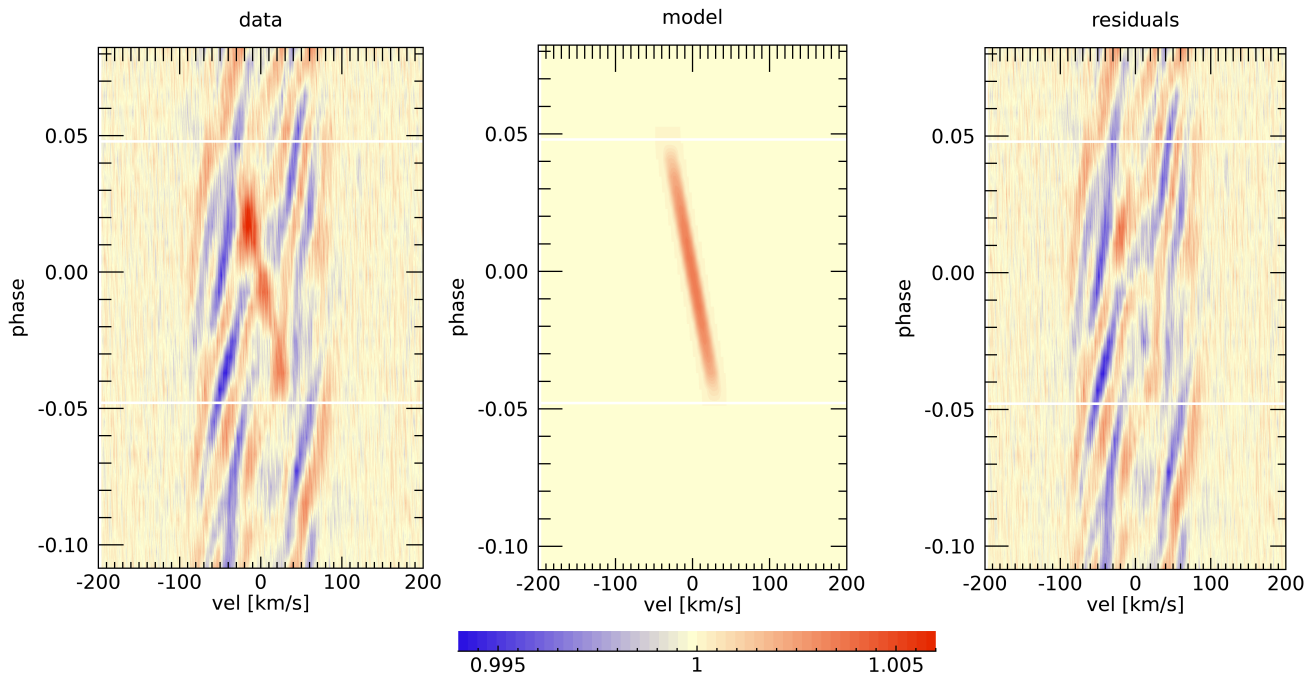


Fig. 5. Example of the removal of the Doppler shadow from the mean line profile residuals for transit 4. (*Left panel*) Original mean line profile residuals. (*Central panel*) Model of the Doppler shadow. (*Right panel*) Mean line profile residuals after the removal of the Doppler shadow. The horizontal white lines show the beginning and end of the transit.

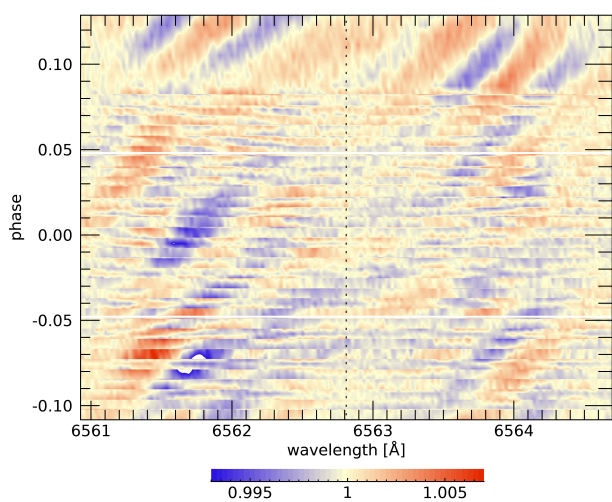


Fig. 6. The effect of the pulsations contamination on the three analysed transits as it affects the $H\alpha$ line, in the stellar restframe. The vertical dotted line marks the position of the $H\alpha$ line. The horizontal white lines show the beginning and end of the transit.

can translate the contrast into an effective planetary radius $R_{\text{eff}} = 1.09 \pm 0.03 R_p$.

We note that the values of absorption depth we obtain are almost half of those obtained for the same planet by Yan et al. (2021) ($0.99 \pm 0.05\%$ for $H\alpha$ and $0.54 \pm 0.07\%$ for $H\beta$, respectively). However, the $H\alpha/H\beta$ line depth ratio is the same (1.93 ± 0.44 for us versus 1.83 ± 0.26 for them). Given the fact that also another analysis of these lines shows different line profile depths ($1.68 \pm 0.02\%$ for $H\alpha$ and $1.02 \pm 0.05\%$ for $H\beta$, Cauley et al. 2021), we highlight the possibility that the amplitude of the lines could be variable with time and with the level of the stellar

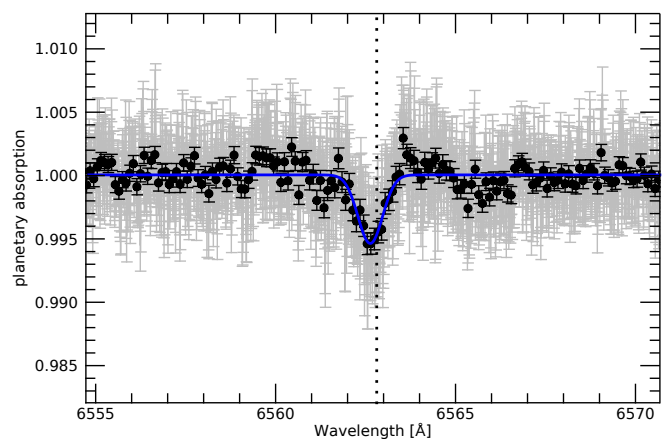


Fig. 7. $H\alpha$ absorption after the correction for stellar effects (RM+CLV and pulsations). Black circles represent 0.1 \AA binning. The blue line is the Gaussian best fit. The vertical dotted line shows the planetary $H\alpha$ restframe.

activity (e.g., Borsa et al. 2021) and/or pulsations. We checked within the dataset we analysed, without finding evidence of significant variability with all the three transits having the same $H\alpha$ contrast.

A future common analysis of all available datasets will help shedding light on the possibility of the observed transit depth variations being related to stellar activity and/or pulsation, rather than caused by systematics between different analyses. Furthermore, such an analysis will enable one to obtain a very high-quality average line profile for each detected Balmer line. These profiles can then be used to constrain the temperature structure of the planetary atmosphere in the 10^{-3} – 10^{-9} bar range (e.g., Fosfati et al. 2020), going beyond the analysis of Yan et al. (2021), who employed an isothermal profile and assumed local thermo-

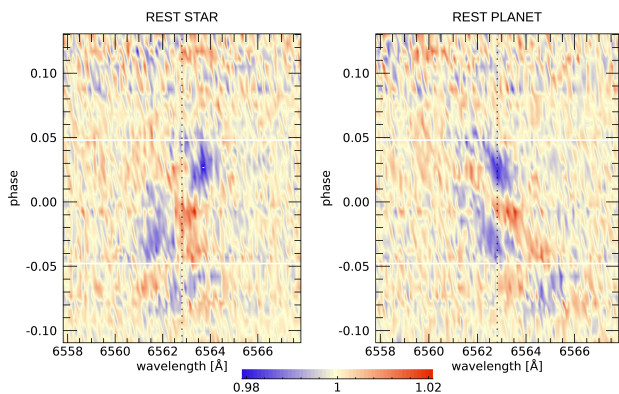


Fig. 8. Contour 2D tomography map of $H\alpha$ absorption in the stellar (left panel) and planetary (right panel) restframes, before applying the stellar contamination correction (this evidences also the Doppler shadow, i.e., the red track). The white horizontal lines represent the beginning and end of the transit. The vertical dotted black line shows the $H\alpha$ planetary restframe in the right panel and the stellar restframe in the left panel. A pre-transit signal, not centered in the planetary restframe, is evident (see discussion in Sect. 6).

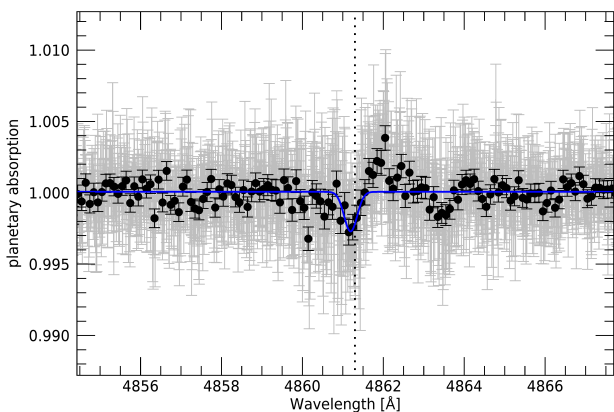


Fig. 9. Same of Fig. 7 but for $H\beta$.

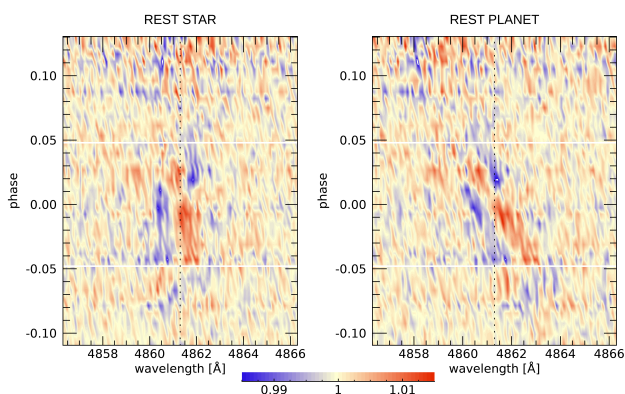


Fig. 10. Same of Fig. 8 but for $H\beta$.

dynamical equilibrium. Indeed, it has been shown that, for modelling the Balmer lines detected in the transmission spectrum of the UHJ KELT-9b, these assumptions are invalid (Fossati et al. 2020). Because of similarities in the temperature profile of the upper atmosphere of KELT-9b and WASP-33b (e.g., both present

a thermal inversion in the upper atmosphere and reach upper atmospheric temperatures of the order of 10000 K; Fossati et al. 2018, 2020), it is likely that the assumptions employed by Yan et al. (2021) for modelling the Balmer lines led them to obtain unreliable results.

6. Pre-transit signal

Looking at the tomographic map of the $H\alpha$ absorption (Fig. 8), we noted a pre-transit feature. This feature has a different slope and duration in the 2D tomographic map with respect to the dominant pulsation pattern in the mean line profiles (see Fig. 1 and Fig. 11). We checked one by one the single transits, and found that this feature looks quite similar in all four available transits (Fig. 11, see the blue diagonal track before the beginning of the transit). It is thus something which happens in an almost coherent timing with the orbital period of the planet.

It appears to be a pseudo-absorption pre-transit signal (PTS hereafter) happening on the stellar surface, because it is moving from $-v \sin i_s$ to $+v \sin i_s$ (i.e., across the stellar CCF) with time. We thus investigated this more in detail, performing the normalization on an extended out-of-transit baseline to avoid including the PTS in it. By visual inspection, we noted that a similar behaviour is observed in many single lines, not only on $H\alpha$. On the mean line profiles it is hidden by the other stellar pulsations, but is still noticeable after removing them (Fig. 1, right panel). Curiously, this feature is also reflected in the radial velocities (see Fig. 3).

We found that the restframe of the PTS is not compatible with the one of the planet, by studying it on the $H\alpha$ line and assuming it is moving with a Keplerian motion around the star with the same orbital period of the planet. Thus we define K_{PTS} as the Keplerian semi-amplitude of this pseudo-orbital motion. By fitting Gaussian functions and maximizing the contrast of their average, we could estimate that the PTS is moving at a $K_{PTS} \sim 460 \text{ km s}^{-1}$ and is centered at phase ~ -0.07 . As averaged on these values, the PTS has a contrast of $0.61 \pm 0.06 \%$ (Fig. 12). Curiously, the value of the K_{PTS} is almost double as the one of K_p (231 km s^{-1} , Table 2). The two shoulders around the profile (Fig. 12) and the red tracks around the signal (Fig. 11) mimic the presence of a Doppler shadow, but this could be possibly due to a normalisation artifact (e.g., Snellen et al. 2010). Yan et al. (2021) do not find any signs of pre-transit absorption in their $H\alpha$ analysis of WASP-33b, but we note that they looked in the planetary restframe only, while we noticed this PTS while looking in the stellar restframe.

Many photometric transit observations of WASP-33b have been gathered (see Sect. 1), and even if they are affected by the stellar pulsations, none of them reported a pre-transit reduction of flux coherent with the planetary orbital period. The most probable option in our opinion is that the PTS is still a stellar pulsation mode, which is possibly/probably excited by the planetary companion just before the transit. The PTS likely belongs to the same pulsations pattern well visible on $H\alpha$ and $H\beta$ lines in Cauley et al. (2021, see their Fig. 5), and also noticeable in Fig. 1, right panel. When averaging different transits the PTS does not average out like the other pulsations, but tends to clearly stand out beyond the noise. This would be indeed evidence of a somewhat expected star-planet interaction for this system. Mechanisms that can excite stellar pulsations could have tidal or magnetic origin.

Planet-induced stellar pulsations were reported for example in the HAT-P-2 system, where de Wit et al. (2017) discovered pulsation modes corresponding to exact harmonics of the

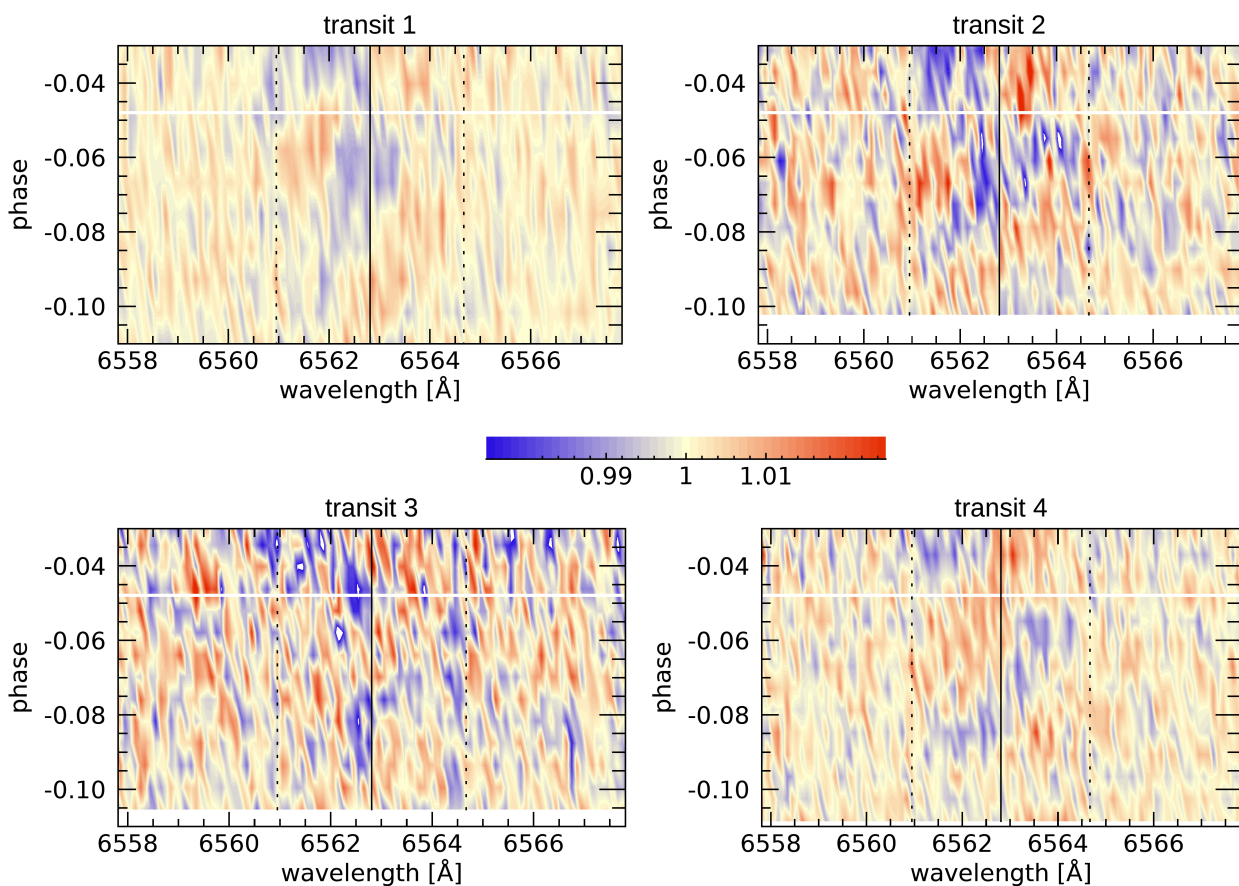


Fig. 11. Zoom on the pre-transit signal on the 4 transits of our dataset, in the stellar restframe. Vertical line shows the $H\alpha$ line center, while vertical dotted lines mark the $\pm v \sin i_s$ limits. Horizontal white line shows the beginning of the transit. The pre-transit signal is the diagonal blue track before the beginning of the transit.

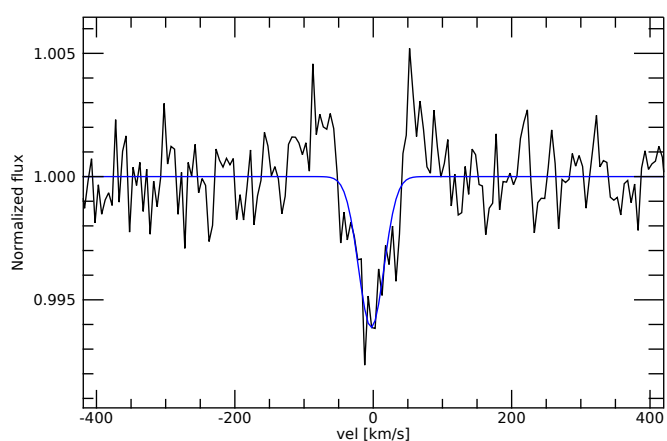


Fig. 12. Pre-transit signal profile in its restframe with $K_{PTS}=460 \text{ km s}^{-1}$. The blue line shows the best-fit Gaussian profile.

planet's orbital frequency, indicative of a tidal origin. Planetary induced tides in the host star, manifesting as the second harmon-

ics of the orbital frequency, were proposed also for the systems WASP-12 and WASP-18 (Maciejewski et al. 2020a,b). Tidally induced flux modulations are also shown in *heartbeat* stars (e.g., Welsh et al. 2011; Thompson et al. 2012), caused by large hydrostatic adjustments due to the strong gravitational distortion they experience during the periastron passage of the eccentric binary companion. We thus can hypothesize a tidal star-planet interaction to be the cause of the PTS. When considering equilibrium tides, we should find two RV maxima/minima during the planetary orbit, but the effect should be of the order of $\sim 10 \text{ m s}^{-1}$ (i.e., lower than the one seen for WASP-18 considering the masses and orbital configuration of the two systems), thus not detectable. When dealing with pulsations excited by tides instead, their amplitude could be much larger, but the lack of a stellar pulsation frequency close to the expected period of tides (~ 1.6 days, assuming a stellar rotational period of 0.884 days and a planetary orbital period of 1.22 days) in the frequencies shown in von Essen et al. (2020) is not in favour of this hypothesis. Moreover, the duration of a resonance between pulsations and tides should be very short with respect to the evolutive timescales of the system. The large oscillations produced by the resonance would in fact dissipate a lot of energy, producing an

exchange of angular momentum between rotational and orbital motion that modifies both, moving the system out of the resonance soon. So the probability that we are observing the system exactly in this moment is low, which is also not favouring the tidal hypothesis.

Another possibility for the detected PTS is that of a magnetic interaction. Magnetic star-planet interaction has been proposed and observed for some short-period systems, mainly as the modulation of stellar activity index with the orbital period (e.g., Lanza 2009, 2012; Strugarek 2018; Cauley et al. 2019). A pre-transit absorption in the Balmer lines was observed for HD 189733b (Cauley et al. 2015) and was proposed as being caused by the planetary magnetic field, with a bow shock forming around the magnetosphere heading ahead of the planet (Llama et al. 2013; Cauley et al. 2015). Magnetic fields are known to have effect on stellar pulsations, depending on their magnitude (e.g., Handler 2013, and references therein). The interesting possibility of the PTS being a magnetic excitation of pulsations given by the interaction with the planetary magnetic field could be further explored with spectro-polarimetric measurements, since magnetic fields affect not only the spectral line profiles but also polarization properties of stellar radiation (e.g., Landi Degl’Innocenti & Landolfi 2004; Oklopčič et al. 2020).

7. Cross-correlation with templates

Since we found the K_{PTS} to be almost double of the planetary K_p (Sect. 6), we tried to test a possible relation of the PTS with the planetary atmosphere, which could have left aliases or reflections/scattering in the spectra after removing the stellar master. We thus looked in our planetary transmission spectrum for species that could be present only in the planet atmosphere and not in the star, to be further investigated in the PTS restframe in case of detection. We decided to look for Vanadium (V I), which has been already detected in an exoplanetary atmosphere and not in the host star (Ben-Yami et al. 2020; Borsa et al. 2021), and for Aluminum oxide (AIO), which has been claimed to be present in the atmosphere of WASP-33b through low-resolution spectrophotometric observations (von Essen et al. 2019).

Planetary atmosphere transmission models were created by using `petitRADTRANS` (pRT, Mollière et al. 2019). We assumed solar abundances, a continuum pressure level of 1 mbar, and an atmospheric temperature-pressure profile calculated for the planet in the same way as presented in Fossati et al. (2020). These parameters were set because they are typical for UHJs (e.g., Hoeijmakers et al. 2019; Stangret et al. 2020). The atmospheric models, created in planetary radius as a function of wavelength, were translated into flux $(R_p/R_s)^2$, convolved at the HARPS-N resolving power and continuum normalized. While for V I we used the opacities already included within pRT, for AIO we used those available at the opacity database of the Exoplanet Simulation Platform¹ (Grimm & Heng 2015), that we arranged in the pRT format.

Cross-correlation between the data and the models was performed in the stellar restframe on single residual spectra after the removal of a master out-of-transit star and telluric contamination (with the procedures explained in Sect. 5) on the whole wavelength range. This was done by working on the bi-dimensional

$e2ds$ HARPS-N spectra order-by-order. We define the cross-correlation as

$$C(v, t) = \sum_{i=1}^N x_i(t, v) T_i \quad (1)$$

where T is the model template normalized to unity and x are the normalized fluxes at the N wavelengths i of the spectra taken at time t and shifted at velocity v . In this way we preserve the flux information (e.g., Hoeijmakers et al. 2019). In our models we impose all the values with contrast less than 5% of the maximum in the wavelength range to be zero.

We selected a step of 1 km s^{-1} and a velocity range $[-300, 300] \text{ km s}^{-1}$, performing the cross-correlation for each order. We performed a 5σ -clipping and masked the wavelength ranges most affected by telluric contamination. Then for each exposure we applied a weighted average between the cross-correlations of the single orders, where the weights applied to each order are the inverse of the standard deviation (i.e., the larger the S/N, the higher the weight) times the depths of the lines in the model template. For a range of K_p values from 0 to 300 km s^{-1} (with steps of 1 km s^{-1}) we averaged the in-transit cross-correlation functions after shifting them in the planetary restframe. This last step is done by subtracting the planetary radial velocity calculated for each spectrum as $v_p = K_p \times \sin 2\pi\phi$, with ϕ the orbital phase. In this way, we created the K_p vs V_{sys} maps, that are used to test the planetary origin of any possible signal. We evaluated the noise by calculating the standard deviation of the K_p vs V_{sys} maps far from where any stellar or planetary signal is expected, in particular where $|V| > 90 \text{ km s}^{-1}$.

We find no evidence supporting the presence in the planetary atmosphere either of V I or AIO, giving upper limits (which are model dependent) of 97 ppm and 17 ppm at the 3σ level, respectively. While for V I we are confident in the accuracy of the line list we used, as it has also already brought a clear detection (Borsa et al. 2021), this is not the case for AIO. We performed injection of our AIO model in our data using the abundance found in the detection by von Essen et al. (2019), and we could recover it with $\sim 14\sigma$ significance. Although we did not find evidence for its presence with the available opacities, once an accurate AIO linelist will be available verifying with high-resolution spectroscopy the claimed presence of AIO in the planetary atmosphere (von Essen et al. 2019) will be possible using this dataset.

8. Summary and conclusions

We provide further evidence that WASP-33 is undergoing nodal precession, finding a precession period of $1108 \pm 19 \text{ yr}$, slightly longer than that determined by Johnson et al. (2015). We also found that the stellar spin is perpendicular to the line of sight, and determined the gravitational quadrupole moment of the star $J_2 = (6.73 \pm 0.22) \times 10^{-5}$, which is in close agreement with the theoretically predicted value of $(6.53 \pm 0.41) \times 10^{-5}$ (e.g., Ragozzine & Wolf 2009). By increasing the time coverage of WASP-33b spectroscopic transit observations it will be possible to constrain even more the precession period and possibly, with the growing precision of new-generation instruments, also to detect relativistic effects (Iorio 2016). It would be important to look for other exoplanets in which we can detect orbital precession (other than WASP-33b and Kepler-13Ab), to increase the statistics and understand if this phenomenon could depend also on the presence of other companions, on the value of the stellar rotation or on the orbital obliquity of the system.

¹ <https://dev.opacity.iterativ.ch/>

We found that stellar pulsations contaminate the extracted transmission spectrum of the planet and proposed a method to detrend it, which can be potentially applied to mitigate also stellar activity. The detected $H\alpha$ absorption in the planetary atmosphere extends up to $\sim 1.18 R_p$, while absorption in Ca II H&K was detected with an effective radius of $\sim 1.56 R_p$ (Yan et al. 2019). This confirms the tendency of Ca II H&K and $H\alpha$ to exist up to the highest layers of the atmospheres of hot Jupiters. The line contrast of the planetary absorption we measured for both $H\alpha$ and $H\beta$ lines is lower than previously found in the literature (Yan et al. 2021; Cauley et al. 2021), while their contrast ratio is the same. This opens the possibility that the atmosphere of WASP-33b could be sensitive to a variable level of activity of the star.

We detected a pre-transit signal almost coherent with the orbital period of the planet. The most likely explanation is that this is a stellar pulsation mode, which is excited by the planetary companion. The nature of this possible star-planet interaction is still doubtful, even if we tend to exclude tidal interactions and are more in favour of possible magnetic interactions. Spectropolarimetric observations of the transit and a complete spectroscopic phase coverage, as well as a detailed analysis of stellar pulsations on the line profiles, could help in understanding the nature of this pre-transit signal.

Acknowledgements. We thank the referee for their useful comments that helped improving the clarity of the manuscript. We acknowledge the support by INAF/Frontiera through the "Progetti Premiali" funding scheme of the Italian Ministry of Education, University, and Research and from PRIN INAF 2019. FB acknowledges financial support from INAF through the ASI-INAF contract 2015-019-R0.

References

- Akinsanmi, B., Barros, S. C. C., Santos, N. C., et al. 2019, *A&A*, 621, A117
- Anderson, D. R., Temple, L. Y., Nielsen, L. D., et al. 2018, arXiv e-prints, arXiv:1809.04897
- Arcangeli, J., Désert, J.-M., Line, M. R., et al. 2018, *ApJ*, 855, L30
- Astudillo-Defru, N., & Rojo, P. 2013, *A&A*, 557, A56
- Ben-Yami, M., Madhusudhan, N., Cabot, S. H. C., et al. 2020, *ApJ*, 897, L5
- Borsa, F., & Zannoni, A. 2018, *A&A*, 617, A134
- Borsa, F., Rainer, M., Bonomo, A. S., et al. 2019, *A&A*, 631, A34
- Borsa, F., Allart, R., Casasayas-Barris, N., et al. 2021, *A&A*, 645, A24
- Broggi, M., de Kok, R. J., Albrecht, S., et al. 2016, *ApJ*, 817, 106
- Casasayas-Barris, N., Palle, E., Yan, F., et al. 2020, *A&A*, 635, A206
- Cauley, P. W., Redfield, S., Jensen, A. G., et al. 2015, *ApJ*, 810, 13
- Cauley, P. W., Shkolnik, E. L., Llama, J., et al. 2019, *Nature Astronomy*, 3, 1128
- Cauley, P. W., Wang, J., Shkolnik, E. L., et al. 2021, arXiv:2010.02118
- Chen, G., Casasayas-Barris, N., Pallé, E., et al. 2020, *A&A*, 635, A171
- Claret, A. 2019, *A&A*, 628, A29
- Claudi, R., Benatti, S., Carleo, I., et al. 2017, *European Physical Journal Plus*, 132, 364
- Collier Cameron, A., Bruce, V. A., Miller, G. R. M., et al. 2010, *MNRAS*, 403, 151
- Collier Cameron, A., Guenther, E., Smalley, B., et al. 2010, *MNRAS*, 407, 507
- Cosentino, R., Lovis, C., Pepe, F., et al. 2012, *Proc. SPIE*, 8446, 84461V
- Cosentino, R., Lovis, C., Pepe, F., et al. 2014, *Proc. SPIE*, 9147, 91478C
- Covino, E., Esposito, M., Barbieri, M., et al. 2013, *A&A*, 554, A28
- Damiani, C., & Lanza, A. F. 2011, *A&A*, 535, A116
- de Wit, J., Lewis, N. K., Knutson, H. A., et al. 2017, *ApJ*, 836, L17
- Donati, J.-F., Semel, M., Carter, B. D., Rees, D. E., & Collier Cameron, A. 1997, *MNRAS*, 291, 658
- Eastman, J., Gaudi, B. S., & Agol, E. 2013, *PASP*, 125, 923
- Eastman, J. 2017, *Astrophysics Source Code Library*, ascl:1710.003
- Eastman, J. D., Rodriguez, J. E., Agol, E., et al. 2019, arXiv:1907.09480
- Fabrycky, D. C., & Winn, J. N. 2009, *ApJ*, 696, 1230
- Fossati, L., Koskinen, T., Lothringer, J. D., et al. 2018, *ApJ*, 868, L30
- Fossati, L., Koskinen, T., France, K., et al. 2018, *AJ*, 155, 113
- Fossati, L., Shulyak, D., Sreejith, A. G., et al. 2020, *A&A*, 643, A131. doi:10.1051/0004-6361/202039061
- Gallet, F., Bolmont, E., Bouvier, J., et al. 2018, *A&A*, 619, A80
- Gray, D.F., 2008, *The Observation and Analysis of Stellar Photospheres*, Cambridge, UK: Cambridge University Press
- Grimm, S. L. & Heng, K. 2015, *ApJ*, 808, 182
- Gustafsson, B., Edvardsson, B., Eriksson, K., et al. 2008, *A&A*, 486, 951
- Handler, G. 2013, *Planets, Stars and Stellar Systems. Volume 4: Stellar Structure and Evolution*, 207
- Haynes, K., Mandell, A. M., Madhusudhan, N., et al. 2015, *ApJ*, 806, 146
- Herman, M. K., de Mooij, E. J. W., Huang, C. X., et al. 2018, *AJ*, 155, 13
- Herman, M. K., de Mooij, E. J. W., Jayawardhana, R., et al. 2020, *AJ*, 160, 93
- Herrero, E., Morales, J. C., Ribas, I., et al. 2011, *A&A*, 526, L10
- Hoeijmakers, H. J., Ehrenreich, D., Kitzmann, D., et al. 2019, *A&A*, 627, A165
- Iorio, L. 2011, *Ap&SS*, 331, 485
- Iorio, L. 2016, *MNRAS*, 455, 207
- Johnson, M. C., Cochran, W. D., Collier Cameron, A., et al. 2015, *ApJ*, 810, L23
- Johnson, M. C., Rodriguez, J. E., Zhou, G., et al. 2018, *AJ*, 155, 100
- Kovács, G., Kovács, T., Hartman, J. D., et al. 2013, *A&A*, 553, A44
- Landi Degl'Innocenti, E., & Landolfi, M. 2004, *Astrophysics and Space Science Library*, Vol. 307, *Polarization in Spectral Lines*
- Lanza, A. F. 2009, *A&A*, 505, 339
- Lanza, A. F. 2012, *A&A*, 544, A23
- Leconte, J., Chabrier, G., Baraffe, I., et al. 2010, *A&A*, 516, A64
- Lehmann, H., Guenther, E., Sebastian, D., et al. 2015, *A&A*, 578, L4
- Llama, J., Vidotto, A. A., Jardine, M., et al. 2013, *MNRAS*, 436, 2179
- Lothringer, J. D., Barman, T., & Koskinen, T. 2018, *ApJ*, 866, 27
- Maciejewski, G., Niedzielski, A., Villaver, E., et al. 2020, *ApJ*, 889, 54
- Maciejewski, G., Knutson, H. A., Howard, A. W., et al. 2020, *Acta Astron.*, 70, 1
- McLaughlin, D. B. 1924, *ApJ*, 60, 22
- Mkrtichian, D. 2015, *IAU General Assembly 29*, 2255391
- Mollière, P., Wardenier, J. P., van Boekel, R., et al. 2019, *A&A*, 627, A67
- Nugroho, S. K., Kawahara, H., Masuda, K., et al. 2017, *AJ*, 154, 221
- Nugroho, S. K., Gibson, N. P., de Mooij, E. J. W., et al. 2020, *ApJ*, 898, L31
- Ogilvie, G. I. 2014, *ARA&A*, 52, 171
- Ohta, Y., Taruya, A., & Suto, Y. 2005, *ApJ*, 622, 1118
- Oklopčić, A., Silva, M., Montero-Camacho, P., et al. 2020, *ApJ*, 890, 88
- Parmentier, V., Line, M. R., Bean, J. L., et al. 2018, *A&A*, 617, A110
- Piskunov, N., Kupka, F., Ryabchikova, T. A., Weiss, W. W., & Jeffery, C. S. 1995, *A&AS*, 112, 525
- Piskunov, N., & Valenti, J. A. 2017, *A&A*, 597, A16
- Ragozzine, D., & Wolf, A. S. 2009, *ApJ*, 698, 1778
- Rainer, M., Poretti, E., Mistò, A., et al. 2016, *AJ*, 152, 207
- Rainer, M., Borsa, F., Pino, L., et al. 2021, *A&A*, 649, A29
- Rossiter, R. A. 1924, *ApJ*, 60, 1
- Rozelot, J. P., Damiani, C., & Pireaux, S. 2009, *ApJ*, 703, 1791
- Ryabchikova, T., Piskunov, N., Kurucz, R. L., et al. 2015, *Phys. Scr.*, 90, 054005
- Smith, A. M. S., Anderson, D. R., Skillen, I., et al. 2011, *MNRAS*, 416, 2096
- Snellen, I. A. G., Albrecht, S., de Mooij, E. J. W., & Le Poole, R. S. 2008, *A&A*, 487, 357
- Snellen, I. A. G., de Kok, R. J., de Mooij, E. J. W., et al. 2010, *Nature*, 465, 1049
- Stangret, M., Casasayas-Barris, N., Pallé, E., et al. 2020, *A&A*, 638, A26
- Strugarek, A. 2018, *Handbook of Exoplanets*, 25
- Szabó, G. M., Pál, A., Derekas, A., et al. 2012, *MNRAS*, 421, L122
- Ter Braak, C. J. F. 2006, *Statistics and Computing*, 16, 239
- Thompson, S. E., Everett, M., Mullally, F., et al. 2012, *ApJ*, 753, 86
- Vidal-Madjar, A., Arnold, L., Ehrenreich, D., et al. 2010, *A&A*, 523, A57
- von Essen, C., Czesla, S., Wolter, U., et al. 2014, *A&A*, 561, A48
- von Essen, C., Mallonn, M., Albrecht, S., et al. 2015, *A&A*, 584, A75
- von Essen, C., Mallonn, M., Welbanks, L., et al. 2019, *A&A*, 622, A71
- von Essen, C., Mallonn, M., Borre, C. C., et al. 2020, *A&A*, 639, A34
- Watanabe, N., Narita, N., & Johnson, M. C. 2020, *PASJ*, 72, 19
- Welsh, W. F., Orosz, J. A., Aerts, C., et al. 2011, *ApJS*, 197, 4
- Wytenbach, A., Ehrenreich, D., Lovis, C., et al. 2015, *A&A*, 577, A62
- Yan, F., Pallé, E., Fosbury, R. A. E., et al. 2017, *A&A*, 603, A73
- Yan, F., Casasayas-Barris, N., Molaverdikhani, K., et al. 2019, *A&A*, 632, A69
- Yan, F., Wytenbach, A., Casasayas-Barris, N., et al. 2021, *A&A*, 645, A22

-
- ¹ INAF – Osservatorio Astronomico di Brera, Via E. Bianchi 46, 23807 Merate (LC), Italy
- ² INAF – Osservatorio Astrofisico di Catania, Via S.Sofia 78, 95123, Catania, Italy
- ³ Dipartimento di Fisica, Università degli Studi di Milano Bicocca, Piazza dell’Ateneo Nuovo, 1, I-20126 Milano, Italy
- ⁴ INAF – Osservatorio Astrofisico di Arcetri, Largo E. Fermi 5, 50125 Firenze, Italy
- ⁵ Space Research Institute, Austrian Academy of Sciences, Schmiedlstrasse 6, A-8042 Graz, Austria
- ⁶ Department of Physics, University of Warwick, Coventry CV4 7AL, UK
- ⁷ INAF – Osservatorio Astrofisico di Torino, Via Osservatorio 20, 10025, Pino Torinese, Italy
- ⁸ Centre for Exoplanets and Habitability, University of Warwick, Gibbet Hill Road, Coventry CV4 7AL, UK
- ⁹ INAF-IAPS Istituto di Astrofisica e Planetologia Spaziali, Via del Fosso del Cavaliere 100, 00133, Roma, Italy
- ¹⁰ INAF – Osservatorio Astronomico di Padova, Vicolo dell’Osservatorio 5, 35122, Padova, Italy
- ¹¹ INAF – Osservatorio Astronomico di Palermo, Piazza del Parlamento, 1, 90134, Palermo, Italy
- ¹² INAF – Osservatorio Astronomico di Trieste, via Tiepolo 11, 34143 Trieste, Italy
- ¹³ Thüringer Landessternwarte Tautenburg, Sternwarte 5, 07778, Tautenburg, Germany
- ¹⁴ Department of Physics, University of Rome Tor Vergata, Via della Ricerca Scientifica 1, I-00133 Rome, Italy
- ¹⁵ Max Planck Institute for Astronomy, Königstuhl 17, D-69117, Heidelberg, Germany
- ¹⁶ Fundación Galileo Galilei - INAF, Rambla José Ana Fernández Pérez 7, 38712 Breña Baja, TF - Spain
- ¹⁷ Instituto de Astrofísica de Canarias (IAC), C/Vía Láctea s/n, 38205 La Laguna, TF - Spain
- ¹⁸ Departamento de Astrofísica, Universidad de La Laguna (ULL), 38206 La Laguna, TF - Spain
- ¹⁹ INAF – Osservatorio Astronomico di Capodimonte, Salita Moiarriello 16, 80131, Napoli, Italy
- ²⁰ INAF – Osservatorio di Cagliari, via della Scienza 5, I-09047 Selargius, CA, Italy
- ²¹ Dip. di Fisica e Astronomia Galileo Galilei – Università di Padova, Vicolo dell’Osservatorio 2, 35122, Padova, Italy

Appendix A: Angular momentum geometry and precession in the WASP-33 system

Appendix A.1: Tidal timescales

The tidal timescales of the decay of the obliquity of the WASP-33 system and the exchange of angular momentum between the stellar spin and the orbit can be estimated using the tidal model of Leconte et al. (2010) that we modify to make use of the stellar and planetary modified tidal quality factors Q'_s and Q'_p , respectively. We adopt $Q'_p = 10^5$, a typical value for a Jupiter-like planet, and $Q'_s = 5 \times 10^6$, that corresponds to a strong tidal coupling as expected in late-type stars, but certainly underestimates the tidal timescales for an A-type star (Ogilvie 2014). Possible resonances between tides and stellar pulsations, that could increase the tidal dissipation inside the star, have been excluded by Kovács et al. (2013).

We find a timescale for the decay of the orbital eccentricity of only 0.2 Myr owing to the strong tidal dissipation enforced by the massive star inside the planet, while the decay of the obliquity and the spin-orbit exchange occur on timescales of ~ 300 Myr and ~ 1 Gyr, respectively, because they depend on the much smaller tidal dissipation inside the star. In conclusion, the precession in WASP-33 can be modelled by assuming that the obliquity and the stellar and orbital angular momenta are of constant magnitude, while the orbit can be assumed to have been already circularized (cf. Damiani & Lanza 2011).

Appendix A.2: Determining the geometry of the system

The obliquity ϵ of the system is the angle between the angular momentum of the orbital motion and the spin of the star and is given by (e.g., Damiani & Lanza 2011; Johnson et al. 2015):

$$\cos \epsilon = \cos i \cos i_s + \sin i \sin i_s \cos \lambda, \quad (\text{A.1})$$

where i is the inclination of the orbital plane, that is, the angle between the line of sight $\hat{\mathbf{k}}$ (i.e., the direction from the observer on the Earth to the barycentre of the system) and the orbital angular momentum \mathbf{l}_{orb} , i_s the inclination of the stellar spin axis to the line of sight, and λ the spin-orbit angle projected onto the plane of the sky, that is measured by fitting the Rossiter-McLaughlin effect or modelling the motion of the Doppler shadow of the planet during its transits. The obliquity ϵ can be assumed constant on the timescales characteristic of the precession (cf. Sect. A.1).

The total angular momentum of the system \mathbf{L}_{tot} is given by the sum of the stellar spin and the orbital angular momentum and is conserved in the absence of external forces (see Fig. A.1). It can be written as:

$$\mathbf{L}_{\text{tot}} = I_s \hat{\boldsymbol{\Omega}}_s + \mathbf{l}_{\text{orb}}, \quad (\text{A.2})$$

where $I_s = M_s (\gamma R_s)^2$ is the moment of inertia of the star of mass M_s , equatorial radius R_s , and gyration radius γ , while $\hat{\boldsymbol{\Omega}}_s$ is the stellar spin angular velocity that is related to the spectral line rotational broadening as $v \sin i_s = \Omega_s R_s \sin i_s$.

The modulus of the total angular momentum can be found by taking the scalar product of eq. (A.2) by itself and considering that $\cos \epsilon = \hat{\boldsymbol{\Omega}}_s \cdot \hat{\mathbf{l}}_{\text{orb}}$:

$$L_{\text{tot}}^2 = I_s^2 \Omega_s^2 + 2I_s \Omega_s l_{\text{orb}} \cos \epsilon + l_{\text{orb}}^2, \quad (\text{A.3})$$

where the modulus of the orbital angular momentum for a circular orbit is:

$$l_{\text{orb}} = mna^2 \quad (\text{A.4})$$

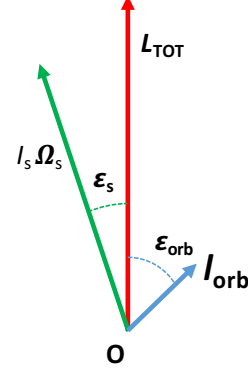


Fig. A.1. The total angular momentum of the system \mathbf{L}_{tot} (in red) as resulting from the composition of the stellar spin angular momentum $I_s \hat{\boldsymbol{\Omega}}_s$ (in green) and the orbital angular momentum \mathbf{l}_{orb} (in blue). The angles ϵ_s and ϵ_{orb} between the stellar spin or the orbital angular momentum and the total angular momentum, respectively, are indicated. The obliquity of the system is $\epsilon = \epsilon_s + \epsilon_{\text{orb}}$, while its projection on the plane of the sky is λ (not indicated).

where $m = M_s M_p / (M_s + M_p)$ is the reduced mass of the system, M_p the mass of the planet, a the semimajor axis of the orbit, and $n = 2\pi/P_{\text{orb}}$ the orbital mean motion with P_{orb} being the orbital period.

Since \mathbf{L}_{tot} is constant, taking the scalar product of eq. (A.2) by the unit vector directed along the line of sight $\hat{\mathbf{k}}$ and making the derivative with respect to the time gives:

$$\frac{di_s}{dt} = -\frac{l_{\text{orb}} \sin i}{I_s \Omega_s \sin i_s} \left(\frac{di}{dt} \right), \quad (\text{A.5})$$

where $\cos i = \hat{\mathbf{k}} \cdot \hat{\mathbf{l}}_{\text{orb}}$ and $\cos i_s = \hat{\mathbf{k}} \cdot \hat{\boldsymbol{\Omega}}_s$.

Taking the time derivative of eq. (A.1), making use of eq. (A.5), and considering the system at the particular epoch when $d\lambda/dt = 0$ and $di/dt \neq 0$ as happened in 2011, we obtain an equation that can be solved for i_s , the inclination of the stellar spin to the line of sight:

$$\frac{l_{\text{orb}} \sin i}{I_s \Omega_s \sin i_s} (\sin i \cos i_s \cos \lambda - \cos i \sin i_s) + \sin i \cos i_s - \cos i \sin i_s \cos \lambda = 0 \quad (\text{A.6})$$

The solution of eq. (A.6) requires a few iterations because Ω_s is derived from the spectroscopic $v \sin i_s$ assuming that the stellar radius R_s is known. The numerical solution converges very rapidly and we adopt the solution closer to $\pi/2$ in our model. In principle, the method can be extended to any epoch when $d\lambda/dt$ and di/dt can both be measured, but the advantage of considering an epoch when $d\lambda/dt = 0$ is that of reducing the errors because the equations simplify and only $di/dt \neq 0$ is required.

To derive the other angles that specify the geometry of the system, we adopt a Cartesian orthogonal reference frame ($Oxyz$) with the origin O at the barycentre of the system, the polar axis $\hat{\mathbf{z}}$ directed along the total angular momentum, and the $\hat{\mathbf{x}}$ axis in the plane defined by the vectors \mathbf{L}_{tot} and the line of sight (cf. Fig. A.2).

We introduce the angle β between the total angular momentum \mathbf{L}_{tot} and the unit vector $\hat{\mathbf{s}}$ directed opposite to the line of sight, i.e., from the barycentre of the system towards the observer, viz. $\hat{\mathbf{s}} \equiv -\hat{\mathbf{k}}$, and $\cos \beta = \hat{\mathbf{L}}_{\text{tot}} \cdot \hat{\mathbf{s}}$. We introduce also the

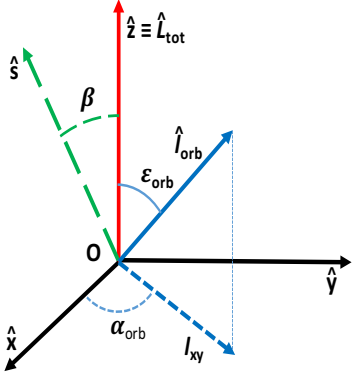


Fig. A.2. Reference frame adopted to specify the geometry of the WASP-33 system. The origin O is at the barycentre of the system; the \hat{z} axis is directed along the total angular momentum of the system (in red); the \hat{x} axis is in the plane defined by the line of sight and the total angular momentum. The vector \hat{s} (dashed in green) is directed opposite to the line of sight, i.e., from the barycentre of the system towards the observer on the Earth. The unit vector in the direction of the orbital angular momentum $\hat{\mathbf{l}}_{\text{orb}}$ is depicted in blue (solid line) together with its projection I_{xy} on the xy plane (dashed line) and the angle α_{orb} between that projection and the \hat{x} axis. The angle α_{orb} varies uniformly in our inertial reference frame due to the precession of the orbital plane (see the text). For simplicity, the stellar spin vector and its projection on the xy plane are not shown.

angles ϵ_s and ϵ_{orb} between the total angular momentum and the stellar spin and orbital angular momentum, respectively, that is, $\cos \epsilon_s = \hat{\mathbf{L}}_{\text{tot}} \cdot \hat{\boldsymbol{\Omega}}_s$ and $\cos \epsilon_{\text{orb}} = \hat{\mathbf{L}}_{\text{tot}} \cdot \hat{\mathbf{l}}_{\text{orb}}$ (see Fig. A.1). In our reference frame

$$\hat{\mathbf{s}} = (\sin \beta, 0, \cos \beta). \quad (\text{A.7})$$

Considering eq. (A.2) and Fig. A.1, we find:

$$\cos \beta = (\hat{\mathbf{s}} \cdot \hat{\mathbf{L}}_{\text{tot}})/L_{\text{tot}} = -(I_s \Omega_s \cos i_s + l_{\text{orb}} \cos i)/L_{\text{tot}}, \quad (\text{A.8})$$

$$\cos \epsilon_s = (\hat{\mathbf{L}}_{\text{tot}} \cdot \hat{\boldsymbol{\Omega}}_s)/(L_{\text{tot}} \Omega_s) = (I_s \Omega_s + l_{\text{orb}} \cos \epsilon)/L_{\text{tot}}, \quad (\text{A.9})$$

$$\cos \epsilon_{\text{orb}} = (\hat{\mathbf{L}}_{\text{tot}} \cdot \hat{\mathbf{l}}_{\text{orb}})/(L_{\text{tot}} l_{\text{orb}}) = (I_s \Omega_s \cos \epsilon + l_{\text{orb}})/L_{\text{tot}}. \quad (\text{A.10})$$

Equations (A.8), (A.9), and (A.10) can be used to find the angles β , ϵ_s , and ϵ_{orb} given that ϵ and i_s have been derived from equations (A.1) and (A.6), L_{tot} comes from eq. (A.3), and the inclination i of the orbital plane is known from the model of the planetary transits.

To complete the description of the system, we need to derive the nodal angles α_s and α_{orb} between the xz plane, defined by the vectors $\hat{\mathbf{L}}_{\text{tot}}$ and $\hat{\mathbf{s}}$, and the spin and the orbital angular momentum, respectively. Since the stellar spin and the orbital angular momentum lie in the same plane containing $\hat{\mathbf{L}}_{\text{tot}}$, $\alpha_s = \pi - \alpha_{\text{orb}}$, so it is sufficient to derive the latter angle. The components of the unit vector directed along $\hat{\mathbf{l}}_{\text{orb}}$ can be expressed as (cf. Fig. A.2):

$$\hat{\mathbf{l}}_{\text{orb}} = (\sin \epsilon_{\text{orb}} \cos \alpha_{\text{orb}}, \sin \epsilon_{\text{orb}} \sin \alpha_{\text{orb}}, \cos \epsilon_{\text{orb}}). \quad (\text{A.11})$$

Considering the definition of the cross product, we have:

$$(\hat{\mathbf{l}}_{\text{orb}} \times \hat{\mathbf{s}})^2 = \sin^2 i. \quad (\text{A.12})$$

Table A.1. The angles and the factor $H(i, \beta, \epsilon, \alpha_{\text{orb}})$ defining the geometry and the rate of nodal precession of the WASP-33 system at the epoch 19 October 2011 when $d\lambda/dt = 0$ is assumed. In addition to the standard deviations giving the statistical errors of the parameters, their systematic deviations obtained by shifting the epoch of $d\lambda/dt = 0$ by 500 days after and before 19 October 2011 are listed, respectively.

	Value [degrees]	Stand. dev. [degrees]	System. dev. [degrees]
i	87.56	0.04	
λ	-114.01	0.22	
ϵ	113.99	0.22	(-0.236; -0.669)
ϵ_{orb}	92.37	2.73	(-0.239; -0.677)
ϵ_s	21.63	2.72	(0.003; 0.008)
i_s	90.11	0.12	(-0.026; -0.015)
β	90.84	0.17	(-0.135; 0.206)
α_{orb}	92.47	0.06	(-0.414; 0.477)
α_s	87.53	0.06	(0.414; -0.477)
$H(i, \beta, \epsilon, \alpha_{\text{orb}})$	-1.0021	0.0024	$(2.1; 3.5) \times 10^{-4}$

By expanding the l.h.s. of eq. (A.12) by means of eqs. (A.7) and (A.11), we obtain an equation for α_{orb} :

$$A \cos^2 \alpha_{\text{orb}} + B \cos \alpha_{\text{orb}} + C = 0, \quad (\text{A.13})$$

where

$$A = \sin^2 \epsilon_{\text{orb}} \sin^2 \beta, \quad (\text{A.14})$$

$$B = \frac{1}{2} \sin(2\beta) \sin(2\epsilon_{\text{orb}}), \quad (\text{A.15})$$

$$C = \sin^2 i - \cos^2 \beta \sin^2 \epsilon_{\text{orb}} - \sin^2 \beta. \quad (\text{A.16})$$

Between the two solutions of eq. (A.13), we choose that giving the correct sign of

$$\cos i = -\hat{\mathbf{s}} \cdot \hat{\mathbf{l}}_{\text{orb}} = -\sin \beta \sin \epsilon_{\text{orb}} \cos \alpha_{\text{orb}} - \cos \beta \cos \epsilon_{\text{orb}}. \quad (\text{A.17})$$

The values of the angles specifying the geometry of the WASP-33 system are listed in Table A.1 together with their standard deviations as obtained by propagating the standard deviations of the system parameters and the systematic deviations obtained by shifting the epoch when $d\lambda/dt = 0$ by 500 days after and before the assumed epoch, respectively.

Appendix A.3: Precession of the orbital plane and the stellar spin

The precession of the orbital plane is described by the precession of the vector $\hat{\mathbf{l}}_{\text{orb}}$ around the total angular momentum $\hat{\mathbf{L}}_{\text{tot}}$. In our reference frame, this precession corresponds to a uniform increase (or decrease) of the nodal angle α_{orb} as a function of the time. We can compute the precession rate by differentiating eq. (A.17) with respect to the time yielding:

$$\frac{d\alpha_{\text{orb}}}{dt} = H(i, \beta, \epsilon, \alpha_{\text{orb}}) \left(\frac{di}{dt} \right). \quad (\text{A.18})$$

where

$$H(i, \beta, \epsilon, \alpha_{\text{orb}}) \equiv -\frac{\sin i}{\sin \beta \sin \epsilon_{\text{orb}} \sin \alpha_{\text{orb}}}. \quad (\text{A.19})$$

The factor $H(i, \beta, \epsilon, \alpha_{\text{orb}})$ is very close to -1 in our system (cf. Table A.1), therefore the rate of nodal precession is virtually

identical in absolute value to di/dt . The minimum and maximum values of the inclination of the orbital plane i , reached along a complete precession cycle, can be obtained from eq. (A.17) for $\alpha_{\text{orb}} = 0, \pi$ and are $\pi - (\beta \pm \epsilon_{\text{orb}})$.

Equation (A.18) can be applied with the observed value of di/dt to provide the observed rate of precession of the nodes of the planetary orbit; the precession period follows as $2\pi/(d\alpha_{\text{orb}}/dt)$. Alternatively, it can be used with the theoretically derived di/dt to predict the expected nodal precession rate in our system. Specifically, the theoretical expression of di/dt for a circular orbit according to eqs. (7) and (11) of Damiani & Lanza (2011) is:

$$\frac{di}{dt} = \mathcal{A}_s \Omega^2 \cos \epsilon \sin i_s \sin \lambda, \quad (\text{A.20})$$

where

$$\mathcal{A}_s \equiv \left(\frac{k_2}{n}\right) \left(1 + \frac{M_p}{M_s}\right) \left(\frac{R_s}{a}\right)^5, \quad (\text{A.21})$$

where k_2 is the apsidal motion constant of the star that depends on its internal density stratification (e.g., Claret 2019). Note that the sign of λ as defined by Damiani & Lanza (2011) is opposite to that adopted by Johnson et al. (2015) and by the present analysis; eq. (A.20) has been reformulated according to the latter convention.

The precession of the stellar spin occurs with the same rate as that of the orbital plane, but in the opposite direction as can be deduced from the conservation of the total angular momentum. The minimum and maximum inclinations of the stellar spin to the line of sight along a precession cycle can be derived as in the case of the orbital plane and are $\pi - (\beta \pm \epsilon_s)$.

Appendix A.4: Gravitational quadrupole moment of the star

The precession rate can be related to the stellar gravitational quadrupole moment J_2 by means of eq. (3) of Johnson et al. (2015) that we recast in our notation as:

$$J_2 = -\frac{1}{3\pi} \frac{P_{\text{orb}}}{\cos \epsilon} \left(\frac{a}{R_s}\right)^2 \left(\frac{d\alpha_{\text{orb}}}{dt}\right). \quad (\text{A.22})$$

Note that our definition of the longitude of the ascending node of the orbit is different from that adopted by Johnson et al., but the precession rate is the same independently of the definition because the precession period is unique for the system.

The gravitational quadrupole moment as derived from the observation of the precession of the orbital plane can be compared with the expectation from the theory. Specifically, J_2 can be described as the sum of the two components $J_{2\text{rot}}$ and $J_{2\text{tide}}$ produced by the centrifugal and the tidal distortion of the star, respectively. Their expressions are (e.g., Ragozzine & Wolf 2009):

$$J_2 = J_{2\text{rot}} + J_{2\text{tide}}, \quad (\text{A.23})$$

$$J_{2\text{rot}} = \frac{2k_2}{3} \left(\frac{\Omega_s^2 R_s^3}{GM_s}\right), \quad (\text{A.24})$$

$$J_{2\text{tide}} = k_2 \left(\frac{M_p}{M_s}\right) \left(\frac{R_s}{a}\right)^3, \quad (\text{A.25})$$

where G is the gravitation constant. In the case of WASP-33, $J_{2\text{tide}} \sim 10^{-3} J_{2\text{rot}}$, therefore it can be neglected in our analysis. Rigorously speaking, eq. (A.25) is valid when the planet is on the equatorial plane of the star, but, given the smallness of $J_{2\text{tide}}$, this conclusion is not affected.

Finally, we note that we have considered the planetary spin synchronized and perpendicular to the orbital plane because tides can enforce such a configuration on a timescale as short as ~ 1 Myr (Leconte et al. 2010). However, if this were not the case, we should include the contribution of the planetary gravitational quadrupole moment to the precession of the orbit as discussed by, e.g., Ragozzine & Wolf (2009) and Damiani & Lanza (2011). General Relativity precession is negligible in our case being ~ 500 times smaller than the nodal precession induced by the oblateness of the star (Iorio 2011).

Appendix A.5: A comparison with the model of Iorio (2016)

Another model of the precession in WASP-33 was presented by Iorio (2016). It assumes a Cartesian reference frame with the y axis directed towards the observer, the z axis along the projection of the stellar spin on the plane of the sky, and the x axis perpendicular to both the other axes to form a right-handed orthogonal coordinate system (see Fig. 1 of Iorio 2016). In such a reference frame, the precession is described through the variation of the angles Ω , the longitude of the ascending node of the orbit measured from the x axis in the x - y plane, and I , the angle between the z axis and the orbital angular momentum. Note that the x - y plane does not coincide with the plane of the sky, while the x - z plane coincides with it.

The two angles Ω and I can be expressed in terms of the inclination i of the orbital plane to the plane of the sky and of the projected obliquity λ on the plane of the sky following equations from (25) to (33) of Iorio (2016) as:

$$\Omega = \arccos \hat{N}_x \text{ for } \hat{N}_y \geq 0 \text{ or} \quad (\text{A.26})$$

$$\Omega = 2\pi - \arccos \hat{N}_x \text{ for } \hat{N}_y < 0, \quad (\text{A.27})$$

where

$$\hat{N}_x = -\frac{\cos i}{\sqrt{\cos^2 i + \sin^2 i \sin^2 \lambda}} \quad (\text{A.28})$$

$$\hat{N}_y = \frac{\sin i \sin \lambda}{\sqrt{\cos^2 i + \sin^2 i \sin^2 \lambda}}, \quad (\text{A.29})$$

while

$$I = \arccos(\sin i \cos \lambda). \quad (\text{A.30})$$

Using the values of i and λ listed by Watanabe et al. (2020) and those derived in the present work, we calculated the angles Ω and I and listed them in Table A.2 together with their standard deviations obtained by propagating the errors on the inclination and the projected obliquity. The only two observations available to Iorio (2016) were those of 2008 and 2014 with the parameters i and λ as reported by Johnson et al. (2015), while we adopted the more precise determination of Watanabe et al. (2020). Therefore, Iorio estimated the rate of precession assuming a constant rate of change for both Ω and I between those two epochs which led to an inclination of the stellar spin axis to the line of sight and a stellar quadrupole moment of, in our notation, $i_s = 142^\circ \pm 11^\circ$ and $J_2 = (2.1 \pm 0.8) \times 10^{-4}$, respectively. Nevertheless, as can be seen in Fig. A.3, the situation was different: the angle I reached a maximum around 2011 and the precession rate dI/dt became zero at that epoch. By differentiating eq. (A.30), we see that dI/dt is zero close to the epoch when $d\lambda/dt = 0$, provided

Day	Month	Year	Ω [degrees]	I [degrees]
12	11	2008	274.00 ± 0.078	111.23 ± 0.48
19	10	2011	272.67 ± 0.041	113.99 ± 0.22
4	10	2014	271.44 ± 0.039	112.90 ± 0.24
28	9	2016	271.11 ± 0.043	111.59 ± 0.26
12	1	2018	270.65 ± 0.059	111.69 ± 0.40
2	1	2019	270.12 ± 0.039	110.83 ± 0.30

Table A.2. The angles Ω and I of the precession model of Iorio (2016) on the epochs of our transit observations.

that i is close to 90° as in the case of a transiting planet, although the two epochs coincide only if $i = 90^\circ$.

Considering eq. (9) of Iorio (2016) and that his unit vector $\mathbf{S}^* = (0, \cos i_s, \sin i_s)$ in our notation, we have for a circular orbit (cf. Section A.1)

$$\frac{dI}{dt} = -\frac{3nJ_2R_s^2}{2a^2} \cos i_s \sin \Omega (\sin i_s \cos I - \cos i_s \cos \Omega \sin I), \quad (\text{A.31})$$

where the symbols have been introduced above. Equation (A.31) for the given values of the angles Ω and I , implies that $dI/dt = 0$ when $\cos i_s = 0$ which confirms our result that the stellar spin is perpendicular to the line of sight around 2011.

The precession rate of the angle Ω at the epoch when $dI/dt = 0$ is given by eq. (10) of Iorio (2016), that is

$$\frac{d\Omega}{dt} = \frac{3nJ_2R_s^2}{2a^2} \cos I \quad (\text{A.32})$$

for a circular orbit. Considering our value of $J_2 = (6.73 \pm 0.22) \times 10^{-5}$, we obtain a precession rate $d\Omega/dt = 0.325 \pm 0.015$ deg/yr in 2011 that is comparable with the observed mean precession rate 0.353 ± 0.007 deg/yr obtained by a linear regression over the six epochs in Table A.2. We do not expect a closer agreement because the precession rate $d\Omega/dt$ is not constant and the angle I is also variable and affected by relatively large errors. Therefore, we prefer to estimate J_2 using equation (3) of Johnson et al. (2015) because in that formula the precession rate and the true obliquity ψ are constant, thus allowing a more precise determination.

In conclusion, the differences between the results of Iorio (2016) and ours as well as those of Watanabe et al. (2020) are due to the paucity of observations available at that time leading to the assumption of constant precession rates for the angles Ω and I . Our more extended dataset allows us to show that the precession rate dI/dt vanished around 2011, thus reconciling our results with those of Iorio's study and confirming that the inclination of the stellar spin axis to the line of sight was very close to 90° at that epoch.

Appendix B: Radial velocities table

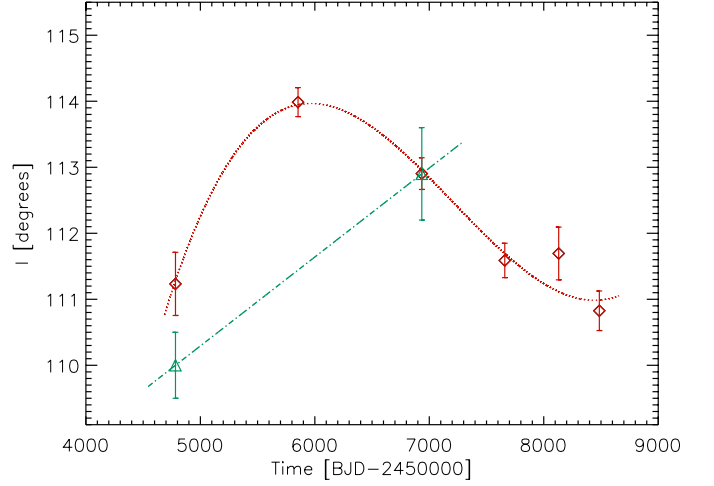


Fig. A.3. The angle I of the model by Iorio (2016) vs. the time. The red diamonds are the values found from our dataset, while the green triangles are the two values derived by Iorio from the data available to him at the time of his work. We see that the precession rate dI/dt is not constant as shown by the cubic interpolation plotted as a dotted red line. For the sake of comparison, we plot a linear interpolation between the two values available to Iorio assuming a constant precession rate.

Table B.1. HARPS-N RV observations of WASP-33.

Time [BJD-2450000]	RV [km s ⁻¹]	RV error [km s ⁻¹]
7660.46966	-2.210	0.137
7660.47683	-2.181	0.148
7660.48443	-2.571	0.178
7660.49131	-3.037	0.194
7660.49830	-3.026	0.224
7660.50580	-2.559	0.235
7660.51275	-1.997	0.221
7660.52008	-1.663	0.202
7660.52736	-2.144	0.222
7660.53481	-2.411	0.216
7660.54183	-2.756	0.172
7660.54914	-2.976	0.190
7660.55612	-3.029	0.173
7660.56343	-2.776	0.137
7660.57031	-2.720	0.132
7660.57806	-2.771	0.166
7660.58493	-2.583	0.187
7660.59189	-2.795	0.201
7660.60012	-3.039	0.176
7660.60686	-2.941	0.155
7660.61359	-2.244	0.173
7660.62139	-1.721	0.207
7660.62879	-1.975	0.177
7660.63575	-2.561	0.174
7660.64275	-2.914	0.175
7660.65028	-3.042	0.155
7660.65731	-2.902	0.156
7660.66485	-2.453	0.148
7660.67192	-2.933	0.143
7660.67904	-3.037	0.155
7660.68626	-3.153	0.156
7660.69377	-3.239	0.159
7660.70097	-3.226	0.150
7660.70797	-2.935	0.151
7660.71520	-2.797	0.160
7660.72256	-3.014	0.165
7660.72983	-3.380	0.168
7660.73690	-3.383	0.157
7660.74419	-3.137	0.158
7660.75355	-3.366	0.144
7682.42344	-2.566	0.111
7682.43060	-2.601	0.118
7682.43791	-2.730	0.129
7682.44515	-2.654	0.121
7682.45238	-2.555	0.122
7682.45945	-2.452	0.144
7682.46686	-2.718	0.164
7682.47396	-3.006	0.152
7682.48140	-2.915	0.160
7682.48844	-2.824	0.153
7682.49562	-2.810	0.147
7682.50304	-3.085	0.148
7682.51000	-2.913	0.170
7682.51738	-2.999	0.163
7682.52458	-2.988	0.177
7682.53171	-2.984	0.171
7682.53903	-2.963	0.167
7682.54636	-2.586	0.185
7682.55371	-2.800	0.220
7682.56072	-2.767	0.217
7682.56810	-2.708	0.208
7682.57520	-2.648	0.188
7682.58247	-2.614	0.199
7682.58974	-2.734	0.183
7682.59696	-2.590	0.164
7682.60426	-2.050	0.166
7682.66575	-3.309	0.191
7682.67303	-3.563	0.170
7682.68015	-3.158	0.159
7682.68730	-2.720	0.143

Table B.1. Continued.

Time [BJD-2450000]	RV [km s ⁻¹]	RV error [km s ⁻¹]
7682.69454	-2.764	0.128
7682.70348	-3.067	0.120
8131.32988	-2.929	0.138
8131.34056	-2.478	0.146
8131.35129	-2.453	0.138
8131.36176	-2.586	0.133
8131.37263	-2.864	0.120
8131.38317	-2.542	0.121
8131.39379	-2.386	0.124
8131.40434	-2.645	0.127
8131.41542	-3.192	0.142
8131.42616	-3.127	0.175
8131.43664	-2.762	0.171
8131.44760	-2.863	0.217
8131.45835	-2.928	0.186
8131.46897	-2.935	0.154
8131.47960	-2.682	0.164
8131.49031	-2.676	0.122
8131.50115	-2.434	0.127
8131.51169	-2.547	0.143
8131.52180	-3.232	0.140
8131.53303	-2.864	0.157
8131.54352	-2.565	0.165
8131.55425	-3.067	0.172
8131.56549	-3.110	0.163
8131.57598	-2.718	0.153
8131.58653	-2.855	0.143
8131.59718	-2.867	0.161
8486.31455	-2.277	0.144
8486.32180	-2.414	0.149
8486.32912	-2.613	0.143
8486.33632	-2.941	0.136
8486.34363	-3.336	0.135
8486.35089	-3.009	0.144
8486.35806	-2.761	0.159
8486.36541	-2.325	0.169
8486.37276	-2.603	0.188
8486.38002	-2.759	0.190
8486.38734	-2.627	0.183
8486.39448	-3.182	0.175
8486.40179	-3.122	0.193
8486.40892	-2.947	0.176
8486.41611	-2.984	0.159
8486.42364	-3.120	0.161
8486.43120	-2.873	0.158
8486.43789	-3.060	0.182
8486.44549	-3.294	0.160
8486.45276	-3.094	0.160
8486.46002	-3.065	0.198
8486.46729	-3.006	0.237
8486.47462	-2.418	0.200
8486.48194	-2.488	0.189
8486.48896	-2.484	0.168
8486.49661	-2.647	0.146
8486.50368	-2.734	0.147
8486.51103	-2.922	0.163
8486.51828	-2.520	0.150
8486.52578	-2.523	0.149
8486.53282	-2.601	0.133
8486.54008	-3.162	0.149
8486.54735	-3.237	0.161